Geochemistry, Geophysics, Geosystems

RESEARCH ARTICLE
10.1029/2020GC009185

Structural Control, Evolution, and Accumulation Rates of Massive Sulfides in the TAG Hydrothermal Field

Sebastian Graber[1], Sven Petersen[1], Isobel Yeo[2], Florent Szitkar[3], Meike Klischies[1], John Jamieson[4], Mark Hannington[1,5], Marcel Rothenbeck[1], Emanuel Wenzlaff[1], Nico Augustin[1], and Iain Stobbs[6]

[1]GEOMAR – Helmholtz-Centre for Ocean Research, Kiel, Germany, [2]National Oceanography Centre, Southampton, UK, [3]Geological Survey of Norway (NGU), Trondheim, Norway, [4]Department of Earth Sciences, Memorial University of Newfoundland, St. John's, Newfoundland and Labrador, Canada, [5]Now at the Department of Earth and Environmental Sciences, University of Ottawa, Ottawa, Ontario, Canada, [6]Ocean and Earth Science, National Oceanography Centre Southampton, University of Southampton, Southampton, UK

Key Points:
- Intersecting fault and fissure populations dominate the structural control of seafloor massive sulfide mineralization
- Ninety percent of the sulfide material is contained in the inactive and weakly active mounds (26 Mt) compared to the high-temperature mound (3 Mt)
- The structural complexity in the TAG area has lead to a large accumulation of sulfide material in a confined area

Supporting Information:
- Supporting Information S1

Correspondence to:
S. Graber,
sgraber@geomar.de

Citation:
Graber, S., Petersen, S., Yeo, I., Szitkar, F., Klischies, M., Jamieson, J., et al. (2020). Structural control, evolution, and accumulation rates of massive sulfides in the TAG hydrothermal field. *Geochemistry, Geophysics, Geosystems*, *21*, e2020GC009185. https://doi.org/10.1029/2020GC009185

Received 19 MAY 2020
Accepted 17 AUG 2020
Accepted article online 24 AUG 2020

Abstract The Trans-Atlantic Geotraverse (TAG) hydrothermal field on the Mid-Atlantic Ridge is one of the best-studied hydrothermal systems to date. However, high-resolution bathymetric data obtained in 2016 by an autonomous underwater vehicle (AUV) reveal new information about the distribution of active and inactive hydrothermal deposits, and their relation to structural features. The discovery of previously undocumented inactive vent sites contributes to a better understanding of the accumulation rates and the resource potential of seafloor massive sulfide deposits at slow-spreading ridges. The interpretation of ship-based and high-resolution AUV-based data sets allowed for the determination of the main tectonic stress regimes that have a first-order control on the location and distribution of past and present hydrothermal activity. The data reveal the importance of cross-cutting lineament populations and temporal variations in the prevalent stress regime. A dozen sulfide mounds contribute to a substantial accumulation of hydrothermal material (~29 Mt). The accumulation rate of ~1,500 t/yr is comparable to those of other modern seafloor vent fields. However, our observations suggest that the TAG segment is different from many other slow-spreading ridge segments in its tectonic complexity, which confines sulfide formation into a relatively small area and is responsible for the longevity of the hydrothermal system and substantial mineral accumulation. The inactive and weakly active mounds contain almost 10 times the amount of material as the active high-temperature mound, providing an important indication of the global resource potential for inactive seafloor massive sulfide deposits.

Plain Language Summary Previously unknown hydrothermal mounds were discovered by an autonomous underwater vehicle in the Trans-Atlantic Geotraverse (TAG) hydrothermal field in the central Atlantic Ocean. The location of the hydrothermal mounds is controlled by crossing fault and fissure populations that have been active at different times. The material in the newly discovered mounds together with that of the previously known mounds accumulates to ~29 Mt of hydrothermal material. Most of the tonnage is contained in inactive or only weakly active mounds where hydrothermal activity has already ceased or is in a waning stage. The hydrothermal activity likely occurs periodically, and we assume an accumulation rate of ~1,500 t/yr, which is comparable to rates from other hydrothermal fields. Within the TAG hydrothermal field, however, the sulfides seem to accumulate over long periods of time and in a relatively small area which is a result of the complex tectonic history of the area.

1. Introduction

Since the discovery of inactive and active massive sulfide chimneys along the East Pacific Rise (Francheteau et al., 1979; Hekinian et al., 1980), these systems and their associated biological communities have been in the focus of international research. Today we know of more than 600 active and inactive sites of hydrothermal venting, either inferred from the detection of hydrothermal plumes (active only) or confirmed from visual ground-truthing (active and inactive) (Beaulieu et al., 2013), with more than 900 additional undiscovered sites estimated to occur along the young mid-ocean spreading ridges (Beaulieu et al., 2015). Seafloor hydrothermal systems play a major role in the input of metals to the ocean, affecting not only chemical but also biological processes (German et al., 2016). Furthermore, seafloor massive sulfide (SMS) deposits,

which form at sites of high-temperature hydrothermal venting, are, together with manganese nodules and cobalt crusts, considered as a possible contribution to the future global metal supply (Cathles, 2011; Hannington et al., 2011; Petersen et al., 2016; Rona, 2003).

Our current understanding of the resource potential of SMS deposits is, however, severely limited by our lack of knowledge about the distribution and size of these deposits. Most of the known marine sulfide occurrences are small (≪1 Mt each; Beaulieu et al., 2013; Hannington et al., 2010), and clusters of larger deposits, a common observation in land-based sulfide districts (Sangster, 1980), have rarely been documented along mid-ocean ridges (Cherkashev et al., 2013; Müller et al., 2018; Rona, Bogdanov, et al., 1993; Rona, Hannington, et al., 1993).

Global resource estimates for SMS deposits are lacking several of the fundamental answers that need to be addressed. There are currently several orders of magnitude between estimates based on observations at the seafloor and those based on calculated metal fluxes (Cathles, 2011; Hannington et al., 2011). In order to produce realistic resource estimates, we must understand how much metal is released by high-temperature fluid convection over a given length of a ridge segment, the specific geological time frame in which it is deposited as massive sulfide, and how much is preserved after hydrothermal activity ceases. Inactive deposits are assumed to be more common and larger than active deposits as they have gone through a full cycle of hydrothermal activity (Jamieson et al., 2014; Van Dover et al., 2018). However, as a consequence of current exploration technologies (i.e., primarily searching for active deposits through investigations of geochemical and geophysical anomalies in the overlying water column), there have been only a few systematic regional surveys for massive sulfide accumulations that target both active and inactive deposits. These recent surveys mainly investigated areas close to the spreading axis using AUVs (Clague et al., 2018; Jamieson et al., 2014; Paduan et al., 2018). Large-scale (tens of square kilometers), high-resolution surveys at a tectonically complex slow-spreading ridge had never been performed. Within the framework of the Blue Mining project, an EU-funded, interdisciplinary project for the development of scientific, technical and legal solutions concerning deep-sea mining, regional survey methods were developed and tested, providing us with the tools to assess the amount and the accumulation rate of sulfides along a significant portion of a slow-spreading mid-ocean ridge segment. In this paper we use ship-based and AUV-based bathymetric data from the TAG hydrothermal field on the central Mid-Atlantic Ridge (MAR) and its geological interpretation to document the distribution of active and inactive hydrothermal mounds in order to investigate the geological processes that govern their location, and, using deposit age data from previous work, to determine deposit growth rates.

1.1. Geological Setting

The TAG hydrothermal field is located at 26°08′N, on a 40-km-long segment of the MAR between the Atlantis Fracture Zone (30°N) and the Kane Fracture Zone (24°N) (Figure 1). Since 2014 this area has been part of the French exploration license area granted by the International Seabed Authority (ISA). The TAG segment is bounded by two right-stepping nontransform discontinuities (NTDs), which offset the ridge axis by about 4–5 km to the east (Purdy et al., 1990; Sempéré et al., 1993). While the segment ends are marked by deep nodal basins, the axial valley floor rises from 4,500 m to about 3,600 m toward the segment center, which is also marked by a decrease in the width of the axial valley from 9 to 6 km (Sempéré et al., 1993).

The TAG segment shows a strong morphological asymmetry between the western and eastern ridge flanks (Zonenshain et al., 1989). The western flank is characterized by axis-parallel ridges and terraces, which are bounded by major normal faults, extending for more than 10 km along axis and accommodate throws of more than 100 m (Kleinrock & Humphris, 1996a; Zonenshain et al., 1989). The eastern flank shows a steeper but smoother morphology and rises to water depths of less than 1,400 m (Karson & Rona, 1990). Widespread parts of the lower eastern flank are covered by mass-wasting deposits (White et al., 1998), with only a small number of exposed scarps in the upper section that define major fault blocks (Karson & Rona, 1990; Zonenshain et al., 1989). No ultramafic material has been found to date; however, Zonenshain et al. (1989) reported the exposure of gabbros and dikes at the eastern flank at water depths of 3,000 m, indicating that vertical movement along the bounding faults was sufficient to expose lower crustal rocks.

The valley floor hosts abundant volcanic centers (Rona, Bogdanov, et al., 1993; Zonenshain et al., 1989). The western half is dominated by hummocky volcanic ridges that are partially covered by sheet flows (Kleinrock et al., 1996; Kleinrock & Humphris, 1996b). In contrast, the eastern section of the valley floor, which hosts

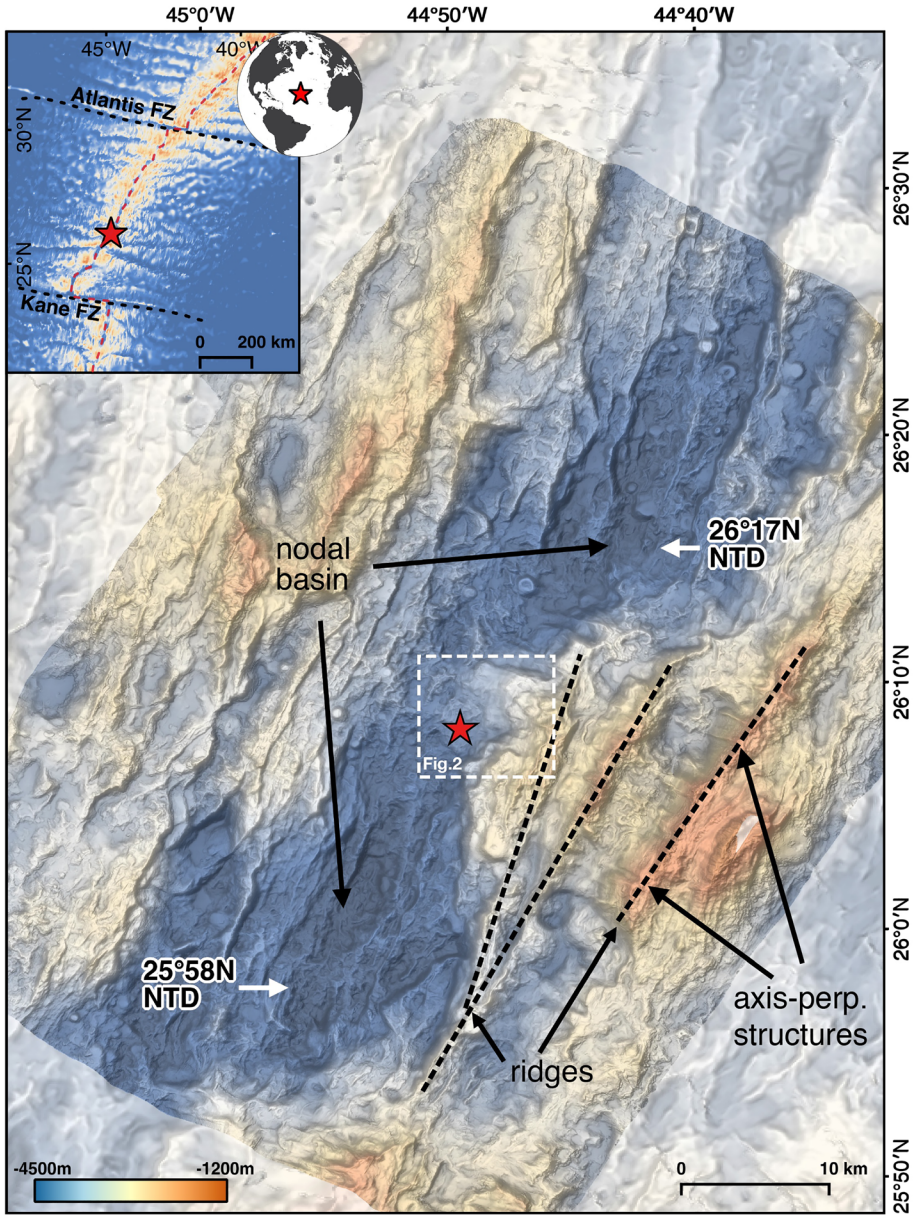

Figure 1. Geological setting and overview of the TAG segment and the TAG hydrothermal field. The inset gives an overview of the central Mid-Atlantic Ridge, showing the location of the active TAG mound (red star) between the Kane and the Atlantis fracture zones (FZ, dashed black lines). The main map displays the slope-shaded ship-based bathymetry (30 m grid resolution) acquired during cruise M127 overlain on the GMRT bathymetry (Ryan et al., 2009). The TAG segment is bounded by two nontransform discontinuities (NTD), which are marked by nodal basins. The eastern flank is characterized by a massif formed by three consecutive ridges (dashed lines). The easternmost ridge shows axis-perpendicular structures on its northwest-facing slope. The outline of Figure 2, showing the AUV bathymetry, is given by the dashed white box.

parts of the hydrothermal field, is a highly tectonized volcanic terrain (Kleinrock & Humphris, 1996b) characterized by dense normal faulting and fissuring (Bohnenstiehl & Kleinrock, 1999; Karson & Rona, 1990).

1.2. The TAG Hydrothermal Field

The TAG hydrothermal field is considered to be basalt-hosted (Rona, Hannington, et al., 1993). However, based on a near-bottom magnetic survey and the occurrence of gabbros on the eastern slope (Zonenshain

et al., 1989), Tivey et al. (2003) suggested that the TAG hydrothermal field lies on the hanging wall of an oceanic detachment fault. Subsequently, several seismic studies (Canales et al., 2007; DeMartin et al., 2007; Schouten et al., 2010; Smith et al., 2008; Zhao et al., 2012) confirmed this and reported the presence of a dome-like fault surface that dips at a steep angle but flattens to about 20° at depths shallower than 3 km below the seafloor under the eastern side of the axial valley. While earlier studies (Canales et al., 2007; DeMartin et al., 2007; Tivey et al., 2003) proposed a young oceanic detachment system, Smith et al. (2008) and Zhao et al. (2012) suggested the presence of an older fault system, extending over 15 km to the east. Therefore, detachment faulting may have shaped the eastern ridge flank for more than 1.35 million years (Zhao et al., 2012).

Early studies of the TAG field described hydrothermal Mn-crusts in a low-temperature zone on the upper eastern flank (Rona, 1976; Rona et al., 1984). Subsequent video-sled surveys documented the active TAG mound on the valley floor (Figure 2), venting hydrothermal fluids with exit temperatures greater than 360°C (Rona et al., 1986). During follow-up side scan sonar, manned submersible and video-sled surveys, several inactive, as well as weakly active mounds, were discovered northeast and east of the active TAG mound (Kleinrock et al., 1996; Lisitsyn et al., 1989; Rona, Bogdanov, et al., 1993; Rona, Hannington, et al., 1993). The Mir Mound, the largest mound structure in the more extensive "Mir Zone" (Rona, Bogdanov, et al., 1993), shows weak signs of hydrothermal activity and is located 2 km ENE of the TAG mound, on an uplifted crustal block (Rona, Hannington, et al., 1993). In the north, several inactive mounds cluster together with another weakly active mound in the so-called "Three Mound area" (southern part of the former "Alvin Zone"). Here, the three large mounds, Southern Mound, which shows evidence for low-temperature fluid flow and associated bacterial mats (Murton et al., 2019), Double Mound (former Alvin Mound) and Shinkai (former New Mound), together with the smaller New Mound 2 and New Mound 3, form a closely spaced group of sulfide occurrences, representing a large accumulation of sulfide material (Figure 2). In 1998 after more than two decades of research in the TAG area, another weakly active low-temperature vent site with sulfide mineralization, called Shimmering Mound, was found 1.5 km north of the Three Mound area (Figure 2a) by side scan sonar and video-sled surveys (White et al., 1998).

Previous studies documented a local tectonic control on the location of the active TAG mound and its association with an intersection of different fault zones, extending from the eastern flank into the valley floor (Karson & Rona, 1990; Kleinrock & Humphris, 1996a). Following the discovery of the detachment fault, Canales et al. (2007) concluded that the hydrothermal field is located in a high-porosity zone in the hanging wall of the detachment fault, where episodic movement along the fault surfaces may have resulted in increased permeability of the hanging wall, periodically reactivating the hydrothermal system and contributing to its longevity (Tivey et al., 2003).

Dating of hydrothermal samples suggests that the hydrothermal activity in the TAG area started about 140 ka ago in the Mir Zone and at 125 ka in the low-temperature zone and later formed sulfide mounds (Three Mound area, TAG active mound, and Shimmering Mound) by episodic hydrothermal activity (Lalou et al., 1986, 1993, 1995). The current phase of high-temperature venting is confined to the active mound and is thought to have initiated nearly 80 years ago (Lalou et al., 1995, 1998).

The heat source driving hydrothermal circulation in the TAG hydrothermal field for the past 140 ka as well as the geometry of the circulation cell are still poorly constrained (Humphris et al., 2015). Both a magmatic body close to 26°06′N (Kong et al., 1992) and heat delivered from the root zone of the detachment several kilometers below the seafloor have been suggested as the possible heat source for the TAG active mound (Canales et al., 2007; DeMartin et al., 2007). Recent studies, however, indicate that the source may be located below the fault (McCaig et al., 2013; Zhao et al., 2012), suggesting that an intrusion into the footwall of the detachment is the most likely heat source for the TAG hydrothermal field (McCaig et al., 2007, 2013; Zhao et al., 2012).

2. Data and Methods

During research cruise M127 on board of RV Meteor in 2016, extensive bathymetric data sets were collected using Meteor's hull-mounted Kongsberg EM122 system, operating at a frequency of 12 kHz, in order to map the entire length of the 26°N segment including the nontransform offsets to the north and south and the off-axis areas (up to 25 km) on each side. The majority of surveys (710 nm in total) were conducted with a

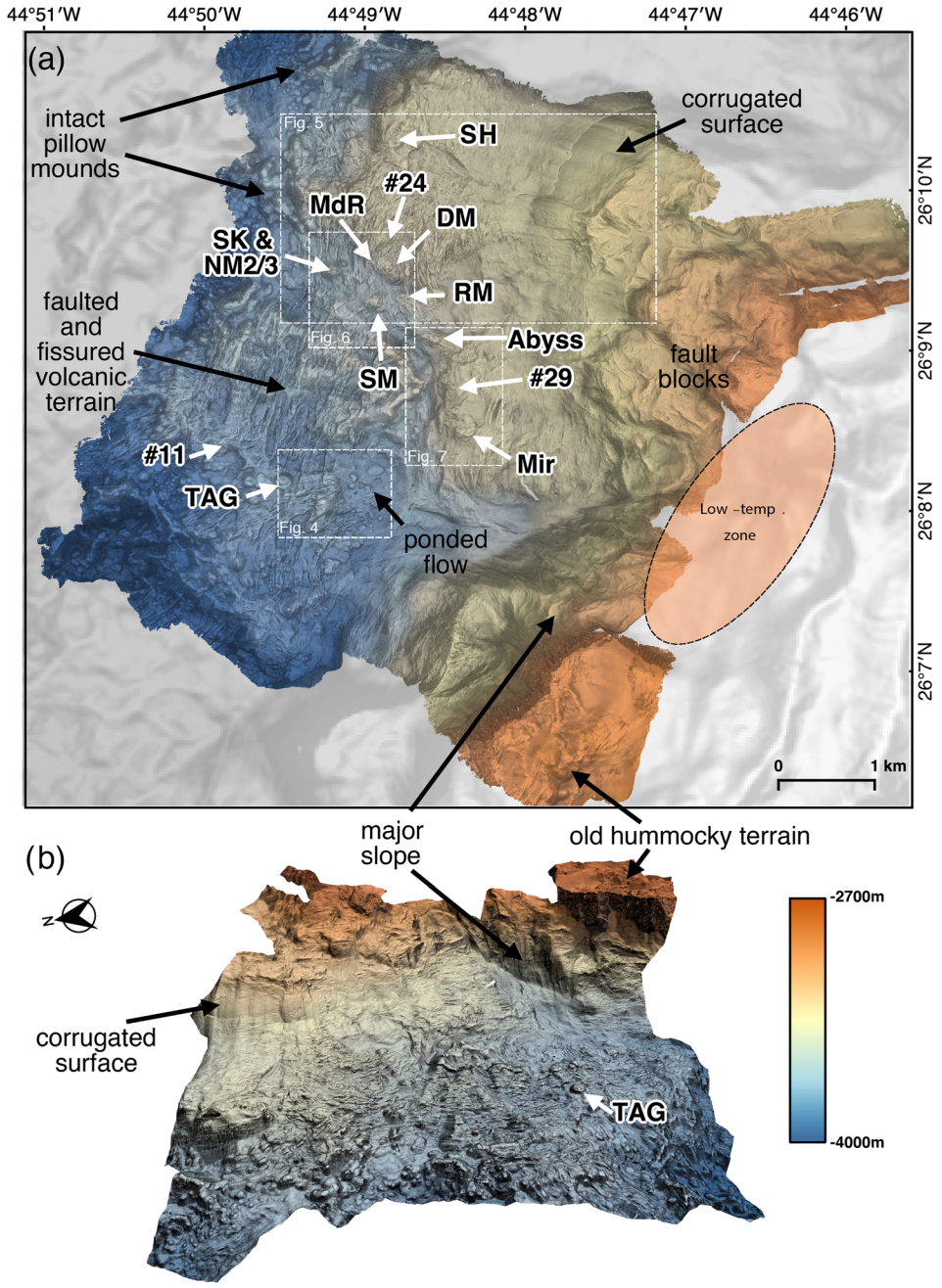

Figure 2. Slope-shaded high-resolution data of the TAG hydrothermal field collected during cruise M127 by the AUV Abyss 6000. (a) High-resolution bathymetry (2 m grid resolution), covering the eastern half of the valley floor, showing hummocky and highly faulted terrain and the adjacent eastern wall characterized by large fault blocks and normal faults. The locations of the hydrothermal mounds are indicated by the white arrows (SH = Shimmering Mound, SM = Southern Mound, RM = Rona Mound, DM = Double Mound, MdR = Mont de Reliques, SK = Shinkai, NM = New Mounds). The orange ellipse shows the approximate location of the low-temperature zone defined in Rona, Hannington, et al. (1993). The dashed white frames show the extent of Figures 4–7. (b) A three-dimensional model of the TAG hydrothermal field (view from the west toward the eastern flank), showing the steep slope in the SE and the rugged morphology in the NE with the adjacent smooth corrugated surface (vertical exaggeration v.e. = 1.5).

symmetrical beam spacing of 45° to both sides (90° full swath angle), a survey speed of 6–8 kn and a line spacing of 3 km, giving a typical swath width on the seafloor of around 7 km and yielding bathymetric grids with a final grid resolution of 30 m. In total, an area of about 4,000 km^2 was mapped by the ship-mounted multibeam system within the study area.

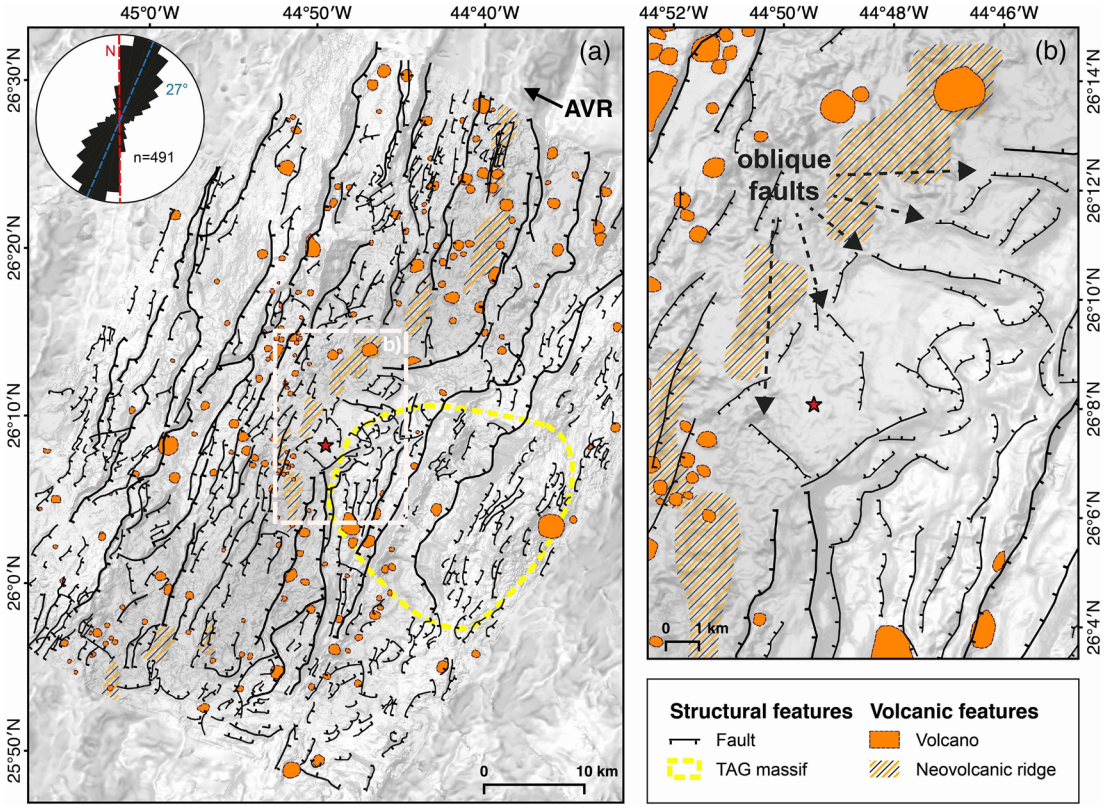

Figure 3. (a) Structural map of the ship-based multibeam bathymetry (slope-shaded over slope-shaded GMRT bathymetry, Ryan et al., 2009). The fault pattern is more complex on the eastern flank. However, most faults follow the overall trend of the spreading axis (rose diagram). The eastern side exhibits fewer \faults of >10 km length, but a higher number of shorter outward dipping faults. The star marks the location of the TAG active mound. The yellow dashed line indicates the outline of the eastern TAG massif. (b) Close-up showing the oblique faults bounding the raised central part of the segment that hosts the TAG hydrothermal field. The location of the close-up is indicated by the dashed white frame in (a).

Additional high-resolution bathymetric data were gathered with the autonomous underwater vehicle (AUV) Abyss 6000 (owned and operated by GEOMAR), which is equipped with a Reson Seabat 7125 multibeam echo sounder. Bathymetric data from 11 AUV dives, using the 200 kHz multibeam configuration, were combined using MB System (Caress, 1999) to create a continuous map over a 7 by 7 km area, with a grid resolution of 2 m, positionally fixed with relation to the location of the well-located drilling reentry cone on the active TAG mound, left behind after the Ocean Drilling Program Leg 158 drilling project (Humphris et al., 1996). More than 47 km^2 of the axial valley and the adjacent lower eastern valley wall were mapped in high-resolution by the AUV. In addition, the Mir Zone and Three Mound area were also mapped at a grid resolution of 50 cm during two missions, using the 400 kHz configuration, at three different altitudes (20, 50, and 80 m). Processing of the raw data was carried out using MB Systems (Caress, 1999), false soundings were removed with QPS Qimera and a digital bathymetric model (DBM) was created with QPS Fledermaus.

A series of criteria derived from the bathymetric data sets were used to define hydrothermal targets and to distinguish them from volcanic mounds. First, slope, surface roughness, and shape in the high-resolution topography data were visually examined in order to identify hydrothermal targets on the seafloor (after Jamieson et al., 2014). Additionally, magnetic lows in the AUV-based magnetic data (Tivey et al., 1993), as well as low backscatter anomalies observed in the ship-based multibeam data, were also considered for the identification of potential targets. Subsequently, the most promising targets were visually inspected using HYBIS, a remotely controlled multi-purpose vehicle (owned and operated by GEOMAR).

2.1. Geological and Structural Mapping

Extensive mapping has been carried out in the area of the TAG segment and the vicinity of the TAG hydrothermal field (Figures 3, 8, and 10). Mapped units and features are primarily defined by their characteristics

Table 1
Overview of the Different Fault Populations Mapped in the Ship-Based (30 m) and High-Resolution (2 m) Bathymetric Data

Data	Faults	Cumulative length (km)	Mean strike (°)	Median strike (°)	Number of faults
Ship-based bathymetry					
	Western flank	896	36.0	29	225
	Eastern flank	816	48.8	35	266
	Total	1,712	42.9	32	491
AUV-based bathymetry					
	Axis-parallel	171	34	24	679
	Oblique	108	68	66	421
	Perpendicular	63.6	134	131	192
	Total	342.6	60	48	1,292

in the bathymetric and backscatter data. To guide the classification of the terrain, derivatives from the DBMs such as slope (angle of inclination), aspect (slope direction), curvature (slope changes), and roughness (topographic variation) were calculated using the open-source software QGIS (v. 3.8.0 Zanzibar; QGIS Development Team, 2019). Structural lineaments were manually mapped as polylines based on the morphological expression in the DBM (an overview is given in Table 1), using the calculated aspect and curvature grids as an aid. Rose diagrams were generated with the QGIS plugin "Line orientation histogram"-plugin (v. 2.6).

2.2. Volume Estimations

Volume calculations for the hydrothermal mounds were conducted in QGIS, by manually defining the outlines of the mound in the high-resolution DBM and subsequently calculating the volume between the actual surface of the mound in the high-resolution data and a reference base. This reference surface is created by inverse-distance weighted (IDW) interpolation based on the terrain along the defined outline and models the original seafloor before the formation of the hydrothermal mounds. We assume that this method is more accurate than using a flat surface at a single depth or an evenly tilted plane as a lower boundary of the mounds (an exemplary figure [Figure S1] for the comparison of the bathymetry and the reference surface of the Mir Mound is included in the supporting information). However, our method does not account for the possibilities that the mounds have formed on top of a smaller volcanic edifice, in a depression or fissure. Due to the irregular shape of the mounds and the rough topography, defining the outlines and extent of the mounds is difficult and the volume and tonnage calculations should be considered as estimates only. A more detailed and precise estimate is, however, only possible by determining the thickness and composition of the interior of the deposits through extensive drilling.

3. Results

3.1. Regional Geological Setting of the TAG Segment

The structural asymmetry between the western and the eastern ridge flanks of the TAG segment is prominent in the ship-based bathymetry. The western flank is characterized by narrow, axis-parallel ridges that extend along-axis for up to 37 km (Figure 1). These ridges are marked by east-southeast dipping normal faults with pronounced fault scarps, which reflect the general trend of the ridge axis (~027°N) (see Figure 3a). In contrast, the topography on the eastern flank is dominated by three axis-parallel ridges that extend over 30 km along axis. The easternmost and largest ridge rises to a water depth of less than 1,400 m. Each of these ridges exhibits prominent northwest facing escarpments. The easternmost ridge shows a smooth northwest dipping slope, which contains a few structures that are parallel to the spreading direction (Figure 1). The origin of these structures is not known. Compared to the fault pattern on the western ridge flank, faulting on the eastern flank is more complex. The large fault systems bounding the three ridges are adjoined by an area to the east that is dominated by smaller faults with varying dipping directions. Transverse, E-W trending faults are observed north of the hydrothermal field on the eastern side of the axis, extending from the flank onto the valley floor, creating a step-like morphology toward the northern NTD (Figure 3b).

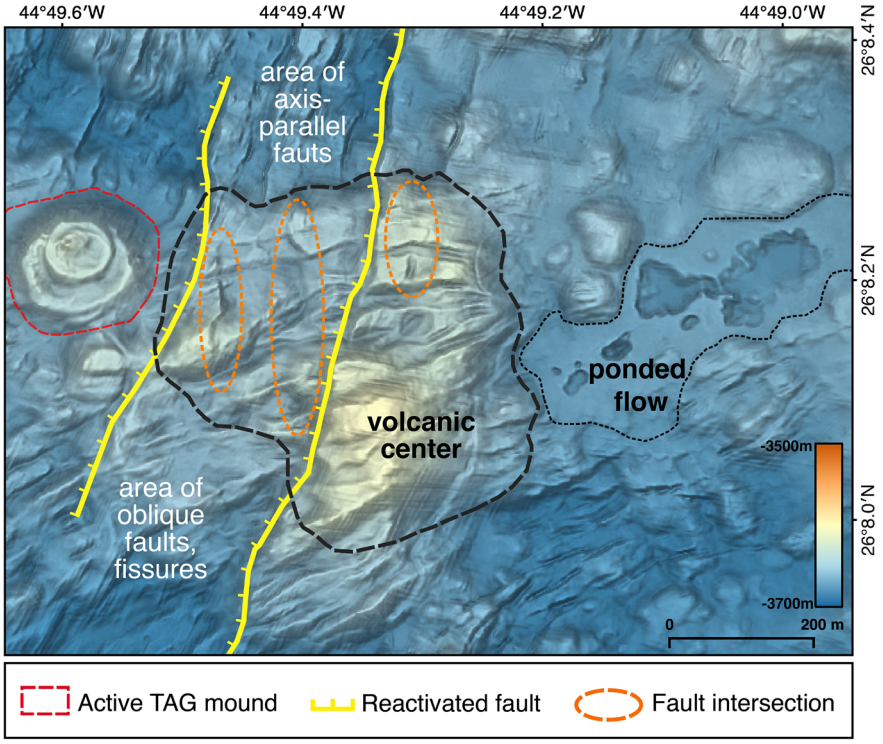

Figure 4. Close-up of the area between the active TAG mound and the Mir Zone (slope-shaded high-resolution [2 m] bathymetry), the adjacent, highly dissected volcanic center (dashed, black line) and the ponded flow in the east (dotted line). The latter shows prominent collapse features and appears to be unaffected by faulting. Two major west dipping faults and the intersection with oblique fissures are highlighted.

The valley floor shows abundant evidence of volcanism in the form of pillow mounds and hummocky ridges, smoother volcanic plains, and small axial volcanoes. A continuous neovolcanic zone cannot be identified along the TAG segment; however, north of the 26°17′N NTD a large axial volcanic ridge (AVR) is apparent that extends for more than 18 km to the north and beyond the area investigated here (Figure 3a). Based on the rough and mostly unfaulted appearance, the hummocky ridges in the center of the axial valley appear to be the areas of most recent volcanic activity and form small neovolcanic ridges, two of which are located 3–4 km west of the active TAG mound (Figure 3b). Small volcanoes are scattered throughout the valley floor but also on both ridge flanks. Flat-top volcanoes occur in a range of sizes from only a few hundred meters to over 2 km in diameter. The hydrothermal vent field, however, is located at the raised eastern half of the valley floor close to the intersection with the eastern bounding wall fault.

3.2. Geological and Structural Setting of the TAG Vent Field

The area of the TAG hydrothermal field, located on the eastern part of the axial valley, was mapped in high resolution by the AUV (Figure 2a). The western half of this area is dominated by pillow mounds. This volcanic terrain stretches from the center of the valley in the west to about 1 km east of the active TAG mound and extends along the entire length of the area mapped by AUV. The southwestern part of the working area, as well as sections west and northwest of the Shinkai mound show intact pillow mounds and smaller hummocky ridges that are not dissected by faulting (see Figure 2a).

In contrast, the central part of the area shows strong axis-parallel lineations caused by extensional faulting, which is restricted to a 1–1.5-km-wide band north of the active TAG mound and a smaller section 500 m to the south (Figure 2a). The regions immediately west and south of the active mound as well as the northwestern corner of the mapped area show signs of a second, cross-cutting fault system that is oblique to perpendicular to the spreading axis, trending northeast-southwest (Figure 4). Therefore, we interpret the active TAG mound to be located at the boundary between an extensional zone in the north and an oblique-fissured zone to the south and west. A small hydrothermal mound (#11) was discovered 750 m

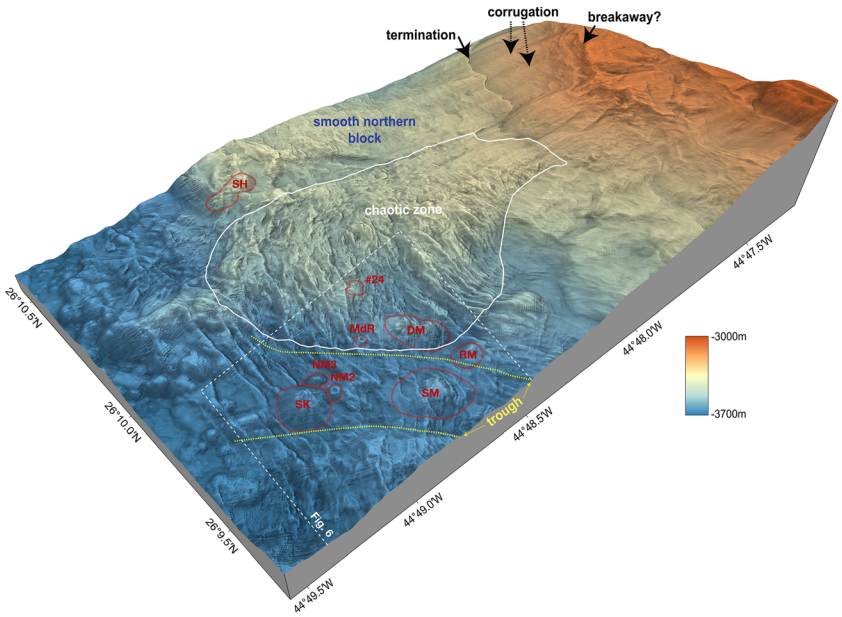

Figure 5. A three-dimensional close-up (slope-shaded 2 m bathymetry) of the northern section of the hydrothermal field comprising the corrugated surface in the northeast and the chaotic zone (indicated by the white line). Several faults extend from the area north of Shinkai and Southern Mound into this chaotic terrain. The elevated northern block shows a rather smooth morphology interrupted only by the Shimmering Mound in the west and the termination of the corrugated surface in the east. The dotted yellow lines indicate the trough, which hosts Shinkai and Southern Mound and separates them from the slightly elevated Double and Rona mounds. The extent of Figure 6 is shown by the dashed white frame (SM = Southern Mound, DM = Double Mound, SK = Shinkai, NM2/3 = New Mound 2/3, SH = Shimmering Mound, MdR = Mont de Reliques, vertical exaggeration v.e. = 1).

west of the active mound, which grew superimposed on a larger volcanic mound (Figure 2a). This mound is covered in hydrothermal material based on a visual inspection and by gravity coring, recovering Fe-Mn-oxyhydroxides (Petersen & Shipboard Scientific Party, 2016). The area east of the active mound is marked by a relict ponded flow which has a smooth surface and exhibits several collapse structures (Figure 4). It lacks any faulting or fracturing, so appears relatively young; however, a sediment cover of several decimeters has been documented by visual inspection, indicating that this ponded lava flow was not formed by a recent volcanic event (Murton et al., 2018). The ponded flow and the area immediately to the north of it, which is formed by unfaulted and unfissured pillow mounds (Figure 4), create an "untectonized island" separating the extensional fault zone in the west from the Mir block in the east.

The southeastern section of the mapped area is characterized by a major slope, extending from water depths of 3,700 to 2,800 m (see Figure 2b). Zonenshain et al. (1989) observed lower crustal rocks in this area; however, different lithologies could not be distinguished in our high-resolution bathymetric data. This major slope is marked by a fault scarp upslope, which forms the boundary to a plateau-like area. This plateau features highly sedimented volcanic hummocks, which are faulted in a northeast-southwest trend and represents the oldest volcanic terrain in the entire area.

The northern section of the survey area is characterized by three distinct areas (Figure 5). A strongly tectonized "chaotic" zone with abundant faults and ridges that show highly variable strike directions, dominates the central region. This area separates the sulfide mound-hosting trough with the Three Mound area in the south from the "smooth northern block". This northern block exhibits a smooth seafloor topography and stretches for 1.8 km from a major westward dipping fault to a corrugated surface in the east. The west facing fault and the associated topographic high hosts the weakly active Shimmering Mound, the northernmost sulfide occurrence in this area. The eastern limit of the smooth northern block is dominated by a sharp ridge, which is inferred to be the termination of a detachment fault (Figure 5). The corrugated surface of this detachment extends for more than 600 m further eastward and extends over a distance of 1.8 km in the

along-axis direction, possibly extending even further north, beyond the area mapped by the AUV. The corrugated surface is bounded by a fault scarp in the east, likely the breakaway of this detachment fault (Figure 5).

3.3. Structural Setting of the Three Mound Area

Mapping of the Three Mound area in 50 cm grid resolution (Figure 6) reveals distinct differences in the topography, age, and geological history of sulfide mounds located in this area. Southern Mound, as well as Shinkai Mound and the small sulfide mounds New Mound 2 and New Mound 3, are hosted within an elongated trough that runs in a NW-SE direction. This trough is heavily dissected and appears to be older than the axis-parallel faulting.

The mounds in the west (Shinkai, New Mound 2, and New Mound 3) appear to be unaffected by the axis-parallel faulting and show relatively smooth, steep slopes (median slopes of 29° for Shinkai Mound; 33° for New Mound 3, and 28° for New Mound 2; Table 2). In contrast, the large Double Mound, located in the chaotic zone (Figure 5) and Southern Mound, which are both located 500 m further to the east, are intensely cut by faults, are sediment-covered (Murton et al., 2019), and their slopes are more gentle (26° and 22°, respectively). Rona Mound, an inactive sulfide mound identified during our cruise M127, is located a further 200 m east of Southern Mound. This mound also shows gentle slopes (median slope of 22°) and is bounded by two opposing faults. The smooth topography and the gentle slope of the mound also contrast with the inactive mounds in the west (e.g., Shinkai) and are more akin to the closer Southern and Double mounds. We, therefore, assume that the low relief mounds in the east are older than the steep-sided mounds to the west. The strike of the faults in the Three Mound area varies from N to ENE, deviating slightly from the general trend of the spreading axis. However, the trends are within the range of regional fault orientations. The dipping directions of the faults reflect a horst and graben system rather than axis-facing normal faults (Figure 6b). The smaller Mont de Reliques and mound #24, which was discovered during M127, are both hosted in the chaotic zone but appear to be unaffected by faulting and might have formed after the dissection of the older Double, Rona, and Southern mounds.

3.4. Structural Setting of the Mir Zone

The Mir Mound is located 2 km ENE of the active TAG mound and was also mapped at 50 cm grid resolution (Figure 7). The mound is located just east of the escarpment of a west facing fault that stretches for over 1 km in a N-S direction (Figure 7b), extending into the trough that runs through the Three Mound area. The extent of the Mir Mound appears to be smaller than previously reported based on the observation of metalliferous sediments during submersible dives (Rona, Hannington, et al., 1993). The mound has an elongated sickle shape and stretches ~400 m in a northwest-southeast direction. The center is marked by a depression, which is connected to the west by an erosional gully (Figure 7c). Standing and toppled chimneys are visible in the bathymetric data in the northern, eastern, and southern parts of the mound. The upper part of the west dipping fault is covered by sulfide talus and chimney fragments resulting in a rough surface texture. The area to the west of the fault is characterized by unfaulted hummocky, volcanic terrain. The areas east and northeast of the Mir Mound are characterized by oblique NNE to NE trending faults and ridges. The origin of a few smaller features and mounds to the SE of the Mir Mound (Figure 7c) cannot be determined by bathymetric observations alone, although their irregular morphology suggests a hydrothermal origin. Two larger targets (Abyss Mound and target #29), which are located along the west facing fault scarp north of the Mir Mound (Figure 7a), were also confirmed to be of hydrothermal origin during a visual survey with the towed HYBIS-system.

3.5. Volume and Tonnage Considerations for the Hydrothermal Mounds

The high-resolution bathymetric data sets offer the opportunity to calculate volumes of the hydrothermal mounds in order to quantify the amount of hydrothermal material amassed along a section of the slow-spreading Mid-Atlantic Ridge (Table 2) and enables us to estimate the accumulation rate over time. To convert volume to tonnage, we have to assume a density for the material. Published density values for individual SMS samples vary between 1.6 and 4.6 t/m^3. For more porous surface sulfides average dry bulk values between 3.1 t/m^3 (Jamieson et al., 2014; Tivey et al., 1999) and 3.6 t/m^3 (Spagnoli et al., 2016) have been used. The most comprehensive set of dry bulk density measurements was performed by Nautilus Minerals for their resource estimate for the Solwara-1 deposit. The dry bulk density of over 400 samples of

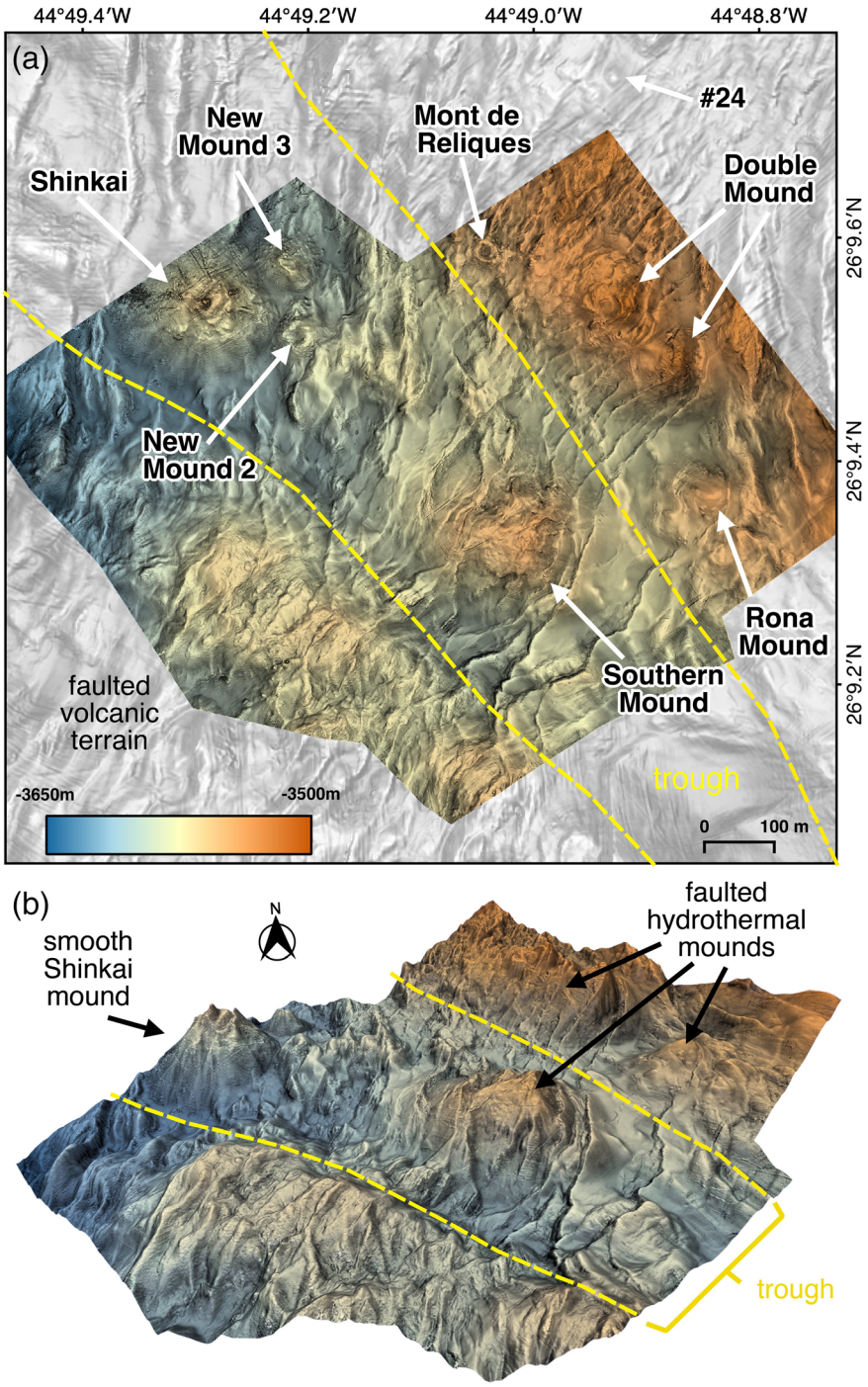

Figure 6. Slope- and terrain texture- (terrain texture Shader, Natural Graphics) shaded high-resolution data of the "Three Mound area" (0.5 m grid resolution). (a) Bathymetry (in map view), covering the highly faulted volcanic valley floor and the vicinity of the major, inactive Shinkai, New Mound 2 and 3, Mont de Reliques, Double Mound as well as Southern and Rona Mound. (b) A three-dimensional model of the "Three Mound area" (v.e. = 1.5). Shinkai and the New Mound 2 and 3 in the west appear smooth and unfaulted, which might indicate a younger age compared to Southern and Double Mound. The latter are highly faulted and fractured by several inward and outward dipping faults. The dashed yellow line indicates the remnants of an older trough in which Shinkai and Southern Mound are located.

Table 2
Location, Characteristics, and Volume Estimate for the Hydrothermal Mounds in the TAG Vent Field

Mound	Latitude	Longitude	Median slope angle (°)	Area (plain) (m^2)	Volume (m^3)	Tonnage (Mt)	Tonnage incl. stockwork (Mt)
TAG active Mound	26°08.22′N	44°49.56′W	25.6	39,693	647,330	2.27	2.95
Mir Mound	26°08.59′N	44°48.44′W	20.2	106,128	1,559,520	5.46	7.10
Southern Mound	26°09.34′N	44°48.98′W	22.1	78,867	1,221,350	4.27	5.56
Shinkai Mound	26°09.54′N	44°49.25′W	29.9	48,938	945,040	3.31	4.30
Double Mound	26°09.50′N	44°48.85′W	26.4	44,126	586,310	2.05	2.67
Shimmering Mound	26°10.34′N	44°48.86′W	26.6	40,792	502,520	1.76	2.29
Abyss Mound	26°09.10′N	44°48.61′W	24.5	36,160	463,840	1.62	2.11
Rona Mound	26°09.37′N	44°48.81′W	22.3	16,501	109,650	0.38	0.50
New Mound 3	26°09.58′N	44°49.18′W	34.7	7,838	76,000	0.27	0.35
Target #29	26°08.81′N	44°48.51′W	27.3	8,584	66,950	0.23	0.30
Target #11	26°08.43′N	44°49.96′W	22.4	11,979	62,000	0.22	0.28
Target #24	26°09.73′N	44°48.90′W	26.0	7,405	40,200	0.14	0.18
New Mound 2	26°09.52′N	44°49.18′W	29.6	4,580	27,440	0.10	0.12
Mont de Reliques	26°09.59′N	44°49.02′W	22.8	2,667	8,900	0.03	0.04
Total				454,258	6,317,050	22.1	28.8

Note. Inactive occurrences are sorted by tonnage. Tonnage estimates for the volume above the reference surfaces are calculated based on a density of 3.5 t/m^3. The second estimate includes a proposed stockwork zone containing an additional 30% of the mound volume (see text for details).

sulfide-dominant rock from drill core averages 3.3 t/m^3 (range from 2.2 to 4.4 t/m^3; Golder Associates Pty. Ltd., 2012). Hannington et al. (1998) used an average density of 3.8 t/m^3 in their assessment of the active TAG mound based on values for dominantly massive, recrystallized pyrite samples drilled from the subseafloor at TAG (Ludwig et al., 1998). As pyrite is likely the dominant sulfide within all inactive mounds in the TAG field (Lehrmann et al., 2018; Murton et al., 2019) we use an intermediate value of 3.5 t/m^3 for our tonnage estimates.

The largest tonnage calculated for the mounds above the reference surface is contained in the Mir Mound (5.5 Mt), followed by Southern Mound (4.3 Mt) and Shinkai Mound (3.3 Mt). For the active TAG mound, although one of the largest known seafloor massive sulfide occurrences, our estimate indicates a tonnage of only 2.3 Mt above the reference surface. Substantial (>1 Mt) sulfide tonnage is also present at Double Mound, Shimmering Mound, and Abyss Mound. The other hydrothermal occurrences do not add significantly to the total tonnage estimate of the study area. Unlike for the newly identified larger sulfide mounds that have been sampled (e.g., Rona Mound and Abyss Mound), it is unclear if the hydrothermal areas from targets #24, #29, and #11 (Figures 2, 5, and 7) are underlain by sulfide material at all. The cumulative tonnage for the entire field is estimated to be 22.1 Mt of sulfide material deposited above our baseline reference surfaces with the largest portion (~90%) contained in the inactive and weakly active mounds.

As no true thickness information is available for the inactive and weakly active mounds, this tonnage estimate has a high degree of associated uncertainty. Our volume calculations assume that the mounds are entirely made up of sulfides. However, it is also possible that these mounds could be composed of sulfide material covering preexisting basaltic pillow mounds. However, the slopes of the mounds, the exposure of massive sulfides along the bounding faults (Murton et al., 2019), and results from drilling into the active TAG mound (Humphris et al., 1996) and the upper few meters of Southern, Rona, and Mir mounds (Lehrmann et al., 2018; Murton et al., 2019) all indicate a hydrothermal origin of at least these mounds. Sulfide accumulation also occurs below the seafloor, mainly within the alteration pipes of the hydrothermal upflow zone where alteration, brecciation, and dissolution enhance permeability and allow for subseafloor precipitation of sulfide minerals, including sulfide veins and replacement of the host rock (Petersen et al., 2000). Based on drilling observations from the active TAG mound where the subseafloor stockwork zone accounts for 30% of the total sulfide tonnage (Hannington et al., 1998) we assume similar proportions for mound/subseafloor tonnage for each of the inactive mounds and add 30% subseafloor sulfides to the tonnage. This will raise the tonnage of the entire TAG vent field to just below 29 Mt.

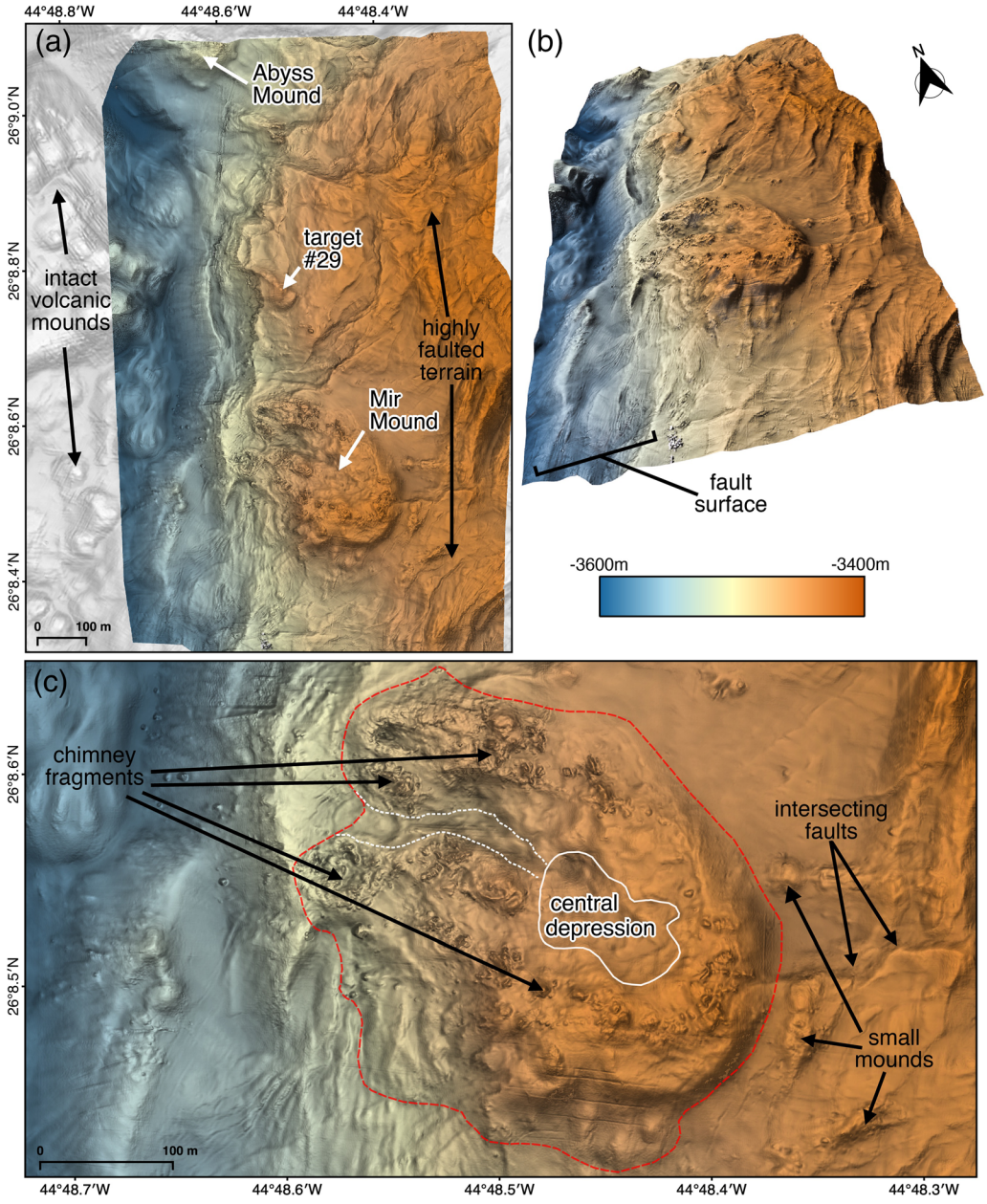

Figure 7. Slope- and terrain texture-shaded high-resolution data of the Mir Zone (0.5 m grid resolution). (a) Bathymetry in map view, stretching from the unfaulted volcanic mounds in the west to the tectonized terrain east of the Mir Zone. (b) A three-dimensional model of the Mir Zone (v.e. = 1.5), the elongated mound can be seen to the east of the steep, westward facing normal fault. The mound shows a rough topography and a roughly elliptical shape. The faults and tectonic ridges to the east of the Mir Mound are also prominent in the 3-D view. (c) Close-up view of the Mir Mound showing remnants of chimneys and the central depression with the westward running erosional gully (dotted, white line).

4. Discussion

4.1. Regional Geological Control

Similar to many other segments on the MAR, the TAG segment is characterized by the interplay of tectonic and magmatic processes (Tucholke & Lin, 1994). However, compared to magmatically robust segments, magmatic accretion at the TAG segment is not focused at the segment center and appears to be more diffuse and distributed along the axis (Zhao et al., 2012). Furthermore, as previous authors have noted, there is a

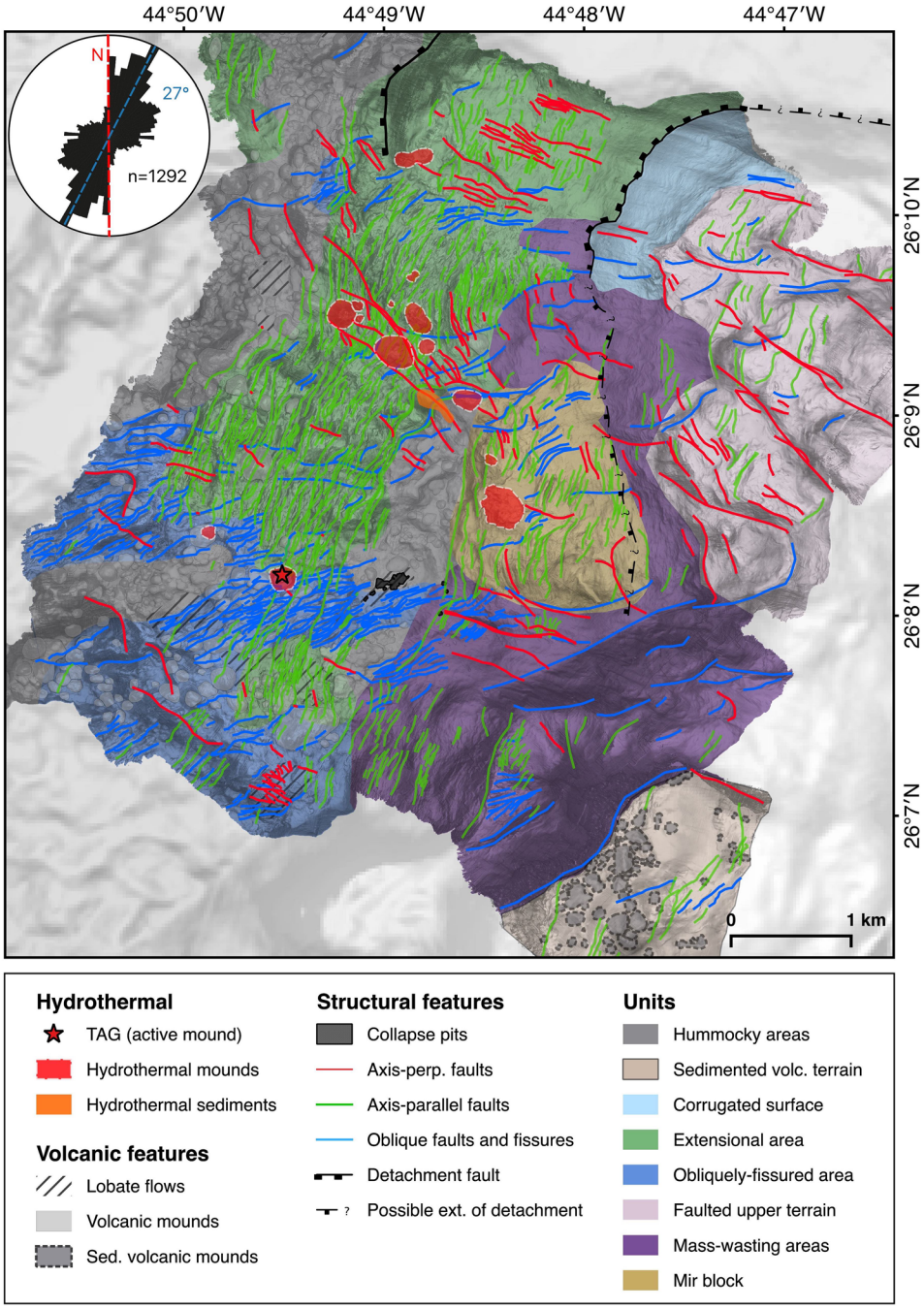

Figure 8. Geological interpretation of the high-resolution AUV bathymetry (2 m) superimposed on slope-shaded 30 m bathymetry). Different lineament populations characterize specific areas within the hanging wall section of the hydrothermal field, while the eastern part is marked by major normal and transfer faults. The rose diagram (upper left) displays the overall trend of all mapped lineaments (*n* indicates the number of lineaments) in 5° divisions, showing a good correlation with the trend of the spreading axis (dashed blue line).

striking asymmetry in this segment of the MAR. The western side is dominated by axis-parallel ridges, terraces, and prominent fault scarps, reflecting the common morphology of slow-spreading ridge crust (Sempéré et al., 1993; Tucholke & Lin, 1994).

Smith et al. (2008) reported bathymetric corrugations from the areas in between the eastern ridges. We could not confirm the proposed corrugations in the off-axis region based on our ship-based bathymetric data with a

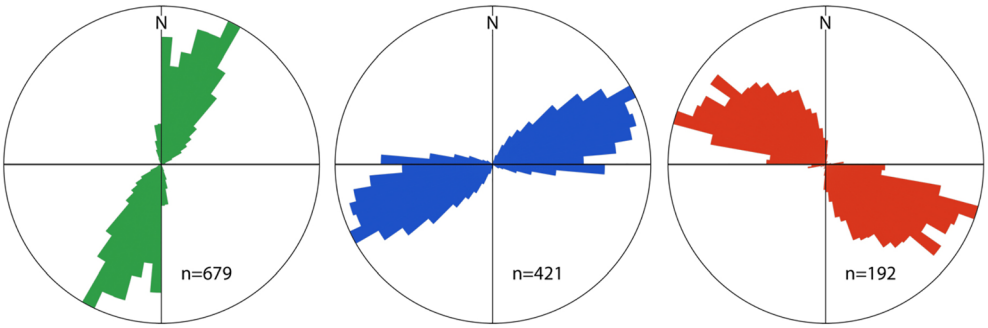

Figure 9. The rose diagram of the 2 m bathymetric data set can be portioned to reflect different groups of lineaments in the TAG area. Axis parallel (green, left), oblique to the axis (blue, middle), and perpendicular to the axis (red, right). These three groups represent different stress and strain regimes and tectonic processes in the evolution of the TAG hydrothermal field (5° divisions).

grid resolution of 30 m, aside from the spreading parallel structures on the steep flank of the easternmost ridge (Figure 1). Some of these structures show similarities to corrugations; however, the slope is steeper (>23°) compared to the typical low-angle dip of other corrugated surfaces in the Atlantic (Escartín et al., 2017; Olive et al., 2019). Furthermore, it should be noted, that the resolution of the older bathymetry, on which the presence of corrugations is based, is coarser than the data presented here. Despite the geophysical evidence, the lack of prominent corrugations contrasts with observations at other detachment systems and OCCs in the Atlantic (Blackman et al., 1998; Escartín et al., 2003; MacLeod et al., 2009; Ranero & Reston, 1999) where extensive corrugated surfaces can be overserved in the ship-based data sets.

An explanation for the absence of major corrugations in our ship-based bathymetric data might be that the eastern ridges are "rider blocks," rafted blocks of the basaltic hanging wall, superimposed on a large detachment structure, covering the fault plane (Schouten et al., 2010; Smith et al., 2008). This type of detachment system is reportedly more common at segment centers and more frequent along the MAR than previously thought (Cann et al., 2015; Reston & Ranero, 2011). However, the branches of the detachment fault that are bounding the rafted blocks have not been imaged by seismic surveys yet. Furthermore, the exact location of the original breakaway is also not known. A large flat-top volcano, located 23 km east-south-east of the active TAG mound, at the eastern flank of the massif (Figure 3), appears to be tilted by more than 15–20° to the east, indicating that the breakaway might be in the eastern section of the massif. An accurate interpretation and classification of the off-axis terrain and the determination of the localization of the original breakaway region are hindered by regional sedimentation at this distance to the spreading axis. Assuming an average sedimentation rate of 1.8 cm/ka (Scott et al., 1978) and the estimated half-spreading rate of between 12 and 13 mm/yr in the east (McGregor et al., 1977; Tivey et al., 2003), the sediment thickness in this area could be more than 30 m, thereby obscuring smaller features and minor fault scarps in the data.

4.2. Local Geological Controls and Implications on the Location of the Hydrothermal Mounds

The high-resolution bathymetry shows a large morphological variability within the hydrothermal field, indicating a strong interplay of tectonic and volcanic processes in the area. The volcanic valley floor is affected to various degrees by faulting and fissuring and can be divided into different structural domains (Figure 8). The center of the hydrothermal field is heavily tectonized and dominated by extensional faulting. We mapped more than 1,200 lineaments in the AUV bathymetry (2 m grid resolution), and the analysis of the strike direction distribution shows three distinct orientation groups (Figure 9) of which the axis-parallel group and the obliquely trending group are confined to certain areas within the hydrothermal field, implying different causes for their formation. The same trends can also be observed in the 50 cm bathymetry of the Three Mound area and Mir Zone (Figure 10). The mapped lineaments in both areas show a strong correlation with the orientation of the spreading axis. However, while the Mir Zone shows only minor secondary peaks in the orientation of the lineaments, the Three Mound area exhibits a strong secondary peak at 10°N, potentially representing an older, deviating fault system associated with the formation of the trough, that runs through the Three Mound area. The intersection of this feature with the different fault populations seems to be one of

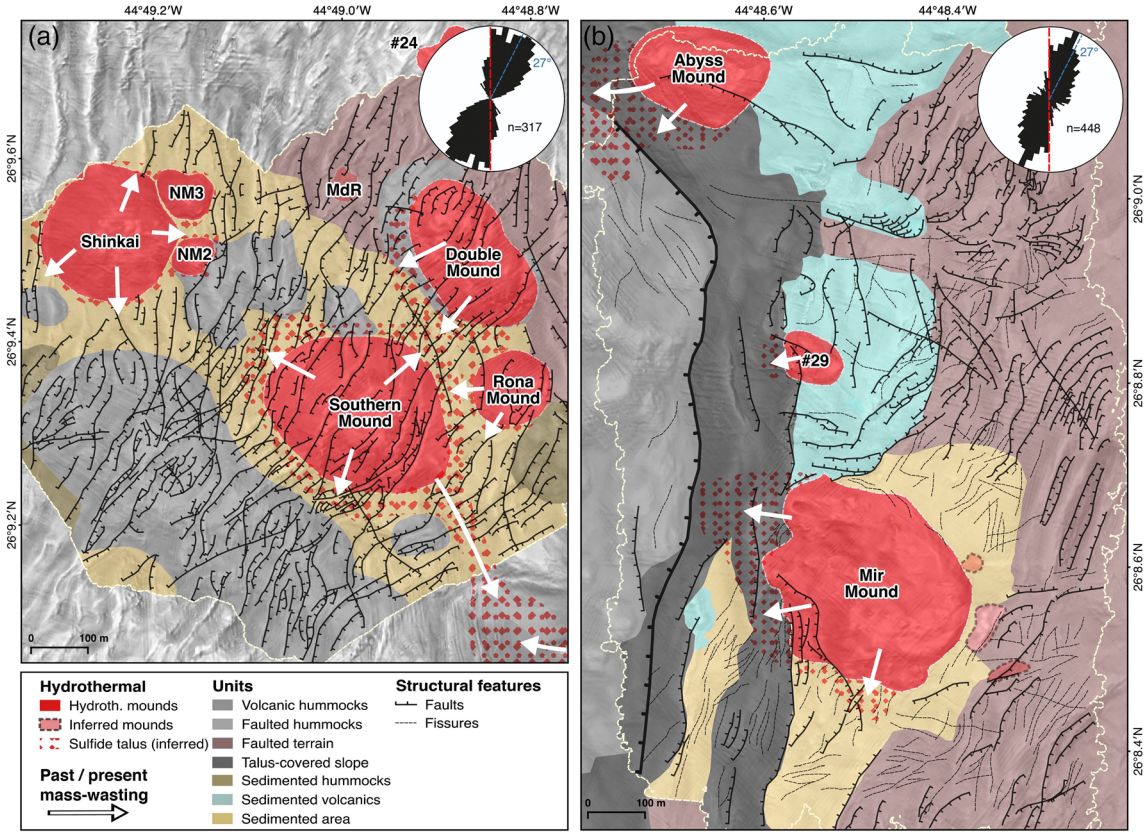

Figure 10. Geological interpretation of the high-resolution bathymetry superimposed on 2 m bathymetry (the extent of the higher-resolution data set is indicated by the dashed white line). (a) The "Three Mound area" is a closely spaced group of three larger as well as several smaller sulfide mounds (MdR = Mont de Reliques, NM = New Mound 2/3) located in a heavily faulted volcanic terrain. The area surrounding the mounds is inferred to be heavily covered by sulfide talus and hydrothermal sediments. The direction of past and present mass movements is indicated by the white arrows. The orientation of the mapped structural features is reflected in the rose diagram (upper right corner, the trend of the ridge axis is indicated by the dashed blue line, n gives the number of lineaments). (b) The sulfide mounds in the Mir Zone are confined to a larger N-S trending fault scarp, extending into the trough, which runs through the "Three Mound area". The upper parts of this slope are covered by sulfides close to the mounds, due to erosion (white arrows indicate mass flows). The Mir Zone is characterized by older faulted volcanic units. However, prominent volcanic mounds can only be recognized west of the major fault in the area north of the ponded flow. The lineament trends of the Mir Zone are displayed by the rose diagram (upper right, *n* indicates the number of lineaments), which shows a good correlation to the spreading axis (dashed blue line) and the trends observed in the 2 m bathymetry.

the main controlling factors for the location of the hydrothermal mounds in the Mir Zone as well as the Three Mound area. Assuming that this trough is an older transfer fault connecting the large bounding fault in the west of the Mir Zone with the northern area, Shimmering Mound might be located on the same larger fault system, that is however partially overprinted by the chaotic zone.

The overall lineament orientations are in good agreement with the trends originally reported by Bohnenstiehl and Kleinrock (1999) from the "fault and fissure zone (FFZ)" in the center of the hydrothermal field and by Bohnenstiehl and Kleinrock (2000) from the vicinity of the active TAG mound. Bohnenstiehl and Kleinrock (1999) indicate that the majority of the extensional faults in the area (>65%; $n = 200$) dip eastward. Our observation deviates slightly from this finding and reflects a horst and graben type of faulting within the extensional zone in the central part of the hydrothermal field.

The active TAG mound and mound #11 occur at the boundary of the extensional zone in the north and the oblique-fissured area in the south (Figure 8). While mound #11 is bounded by relatively unfissured, intact volcanic terrain to the south, the active mound is located on the northwestern side of a larger pillow mound terrain, which is cut by several axis-parallel, west facing faults and some smaller oblique ones (Figure 4). Two major, axis-parallel faults occur within 400 m east of the active mound and extend toward the trough in the north, where they bend east just 200 m south of Southern Mound. These faults were already

reported by White et al. (1998) and are, based on the cross-cutting relationships, either younger faults or reflect the rejuvenation of older extensional faults in the center of the hydrothermal field. Our observations show that some of the axis-parallel faults are cut by the oblique faults, indicating that the development of the oblique faults followed extension (Figure 4). However, the two large, axis-parallel faults near TAG offset the oblique faults. This implies that multiple phases of extensional faulting and oblique fracture development occurred within the hydrothermal field.

Nonetheless, our interpretation of alternating phases of faulting and fissuring deviates from Kleinrock and Humphris (1996a), who proposed that the oblique fissures were preexisting before the initiation of extensional faulting. These oblique fissures are most likely not associated with extensional faulting as they deviate from the general trend of the spreading axis by more than 40°. However, this deviation of the stress regime is interpreted to be localized because the oblique trend is not present within the entire southern part of the area mapped by the AUV. As previously mentioned, "islands" of unfaulted pillow mound terrain, as well as a smaller section of axis-parallel faulted volcanic terrain, are present in the south. The cause of the oblique trend seems to be confined to smaller sections and corridors in the south and north of the area. Bohnenstiehl and Kleinrock (2000) suggested shallow, laterally propagating dikes and the resulting temporal rotation of the stress field as a source for the oblique lineament population, which is known from other spreading zones (Gudmundsson, 1990, 1998) and mainly occurs during episodes of high magmatic activity and dike emplacement. The dominance of the far-field tectonic stress, associated with the plate movement might prevail after a period during which the strain of the dike emplacement dissipates. Such dikes may originate at the spreading axis south of the area mapped here by the AUV, where neovolcanic ridges can be observed in the ship-based multibeam data (Figure 3). Such volcanic centers and hummocky ridges are commonly fed by fissure eruptions related to major diking events. Bohnenstiehl and Kleinrock (2000) suggest that secondary dikes originated from on-axis fissure eruptions might be sufficient enough to induce axis-oblique fissuring, but they also reported that only 1% of the observed fissures in the vicinity of the active mound show any association with volcanic extrusives.

Another explanation for the oblique trend might be the accommodation zone proposed by Karson and Rona (1990). Even though there is no clear structure extending from the flank onto the hanging wall, structural features (fault scarps and smaller faults) show contrasting orientations between the northern section and the major slope south of the Mir block. Furthermore, a few fault lines on the lower flank show similar oblique trends to the valley floor, which might indicate that the deviating stress-field was also present during the time of the formation of the eastern flank and that there is a larger regional-scale influence not related to the intrusion and propagation of dikes.

4.3. Implications for Hydrothermal Convection

Humphris et al. (2015) emphasize that the geometry of the convection cell under the hydrothermal system is still not well understood. The location of the weakly active and inactive sulfide mounds along the N-S trending fault at Shimmering Mound, the slightly curved NW-SE trending trough in the Three Mound area, that extends into the N-S trending fault in the west of the Mir Zone, along with the absence of a magma chamber in the vicinity of the hydrothermal field (Canales et al., 2007), seems to favor an interpretation where hydrothermal fluids are fed by convection driven by a regional heat source at depth and where multiple upflow zones develop in response to the opening of local pathways. This is in agreement with the age dating by Lalou et al. (1995) that indicates simultaneous high-temperature activity not only at the active TAG mound but also at Double Mound. This model explains the widespread distribution of sulfide mounds of various ages, the presence of current low-temperature activity at several mounds, and the focus of high-temperature venting solely at the active mound to date.

The different stages of erosion and tectonic faulting of the sulfide mounds indicate that the location of the upflow zones is changing over time, likely in response to movement along the dominant faults in the specific areas. The diversion of hydrothermal fluids may be further facilitated by the intersection of the faults with past or present-day low-angle detachment faults at depth, which might increase the permeability of the hanging wall (McCaig et al., 2013).

The prominent corrugated surface that is visible in the northeast part of the AUV-based high-resolution map marks the presence of a detachment fault, indicating that a significant portion of the spreading in this area is

accommodated by tectonic movement. This corrugated surface can be traced in seismic data for several kilometers, dipping at a shallow angle, toward the spreading axis in the west, where it seems to be bounded by another detachment fault (Szitkar et al., 2019). The relation between the corrugated detachment fault and the proposed major detachment structure at depth that is supposed to extend further to the east (Schouten et al., 2010; Smith et al., 2008; Zhao et al., 2012) cannot be determined based on our data sets alone. However, it is unlikely that the corrugated surface visible in our AUV data is the upper exposed part of the detachment surface proposed by previous studies, as that surface is thought to be at a depth of 1 km beneath the TAG active mound, steepens toward the center of the axial valley, 2–3 km west of the active Mound (Canales et al., 2007; DeMartin et al., 2007), and dips at a much higher angle compared to the low-angle detachment fault associated with the corrugated surface. This implies that the corrugated surface is either superimposed over a larger detachment faults at depth or that the northern part of the hydrothermal field is structurally different from the southern part as suggested by Szitkar et al. (2019). The TAG massif and especially its western part seems to be highly complex and might be formed by a sequence of detachment faults.

The chaotic zone enclosed by the corrugated surface in the east, Shimmering Mound in the northwest, and the Three Mound area in the south (Figure 5) appears to be an important area to understand the different crustal processes between the northern and southern section of the mapped area. This part of the eastern flank has been interpreted to be related to large mass-wasting events (White et al., 1998). However, it cannot be excluded, that the ridges observed in our high-resolution data are instead related to faulting. Several faults and fractures extend into this region, suggesting that it is unlikely that this terrain formed purely by debris flows from the upper flanks further to the east (Figure 5). Importantly, there is also no prominent concave headwall scarp visible upslope, which would be necessary to produce such an extensive debris fan with a length of almost 2 km and heights of the individual ridges of more than 25 m. Such scars were reported from landslides in the area of the Krasnov and Ashadze hydrothermal fields in the Atlantic (Cannat et al., 2013). Even though a tectonic overprinting of an older debris field cannot be ruled out, a tectonic origin for the chaotic zone seems likely, based on the high-resolution topography. This agrees with the interpretation of high-resolution magnetic data, acquired during our AUV surveys, that led Szitkar et al. (2019) to highlight this location as a "transition zone" between crustal blocks of large differences in tilt.

Even though the heat source driving activity at the active TAG mound might be located beneath the southern part of the hydrothermal field, the lateral extent of the various upflow zones could also span to the area north of Shimmering Mound and the corrugated surface. Unfortunately, we do not have any high-resolution data from this area, and no sulfide occurrences north of Shimmering Mound and the smooth northern block are known to date. Also, stepping further off-axis with high-resolution surveys beyond the Mir Zone did not result in the discovery of additional sulfide occurrences, as most mounds were found close to the intersection of the valley floor with the eastern bounding fault or on the hanging wall section in the western part of the mapped area. The clustering of all known sulfide mounds in a relatively small area and their relative youthfulness (~100,000 years) in comparison to the long evolutional history of the eastern rift valley flank is intriguing. It should be noted, however, that the areal extent of our survey is limited and it cannot be excluded that similarly favorable conditions occurred outside our working area and between the eastern ridges of the TAG massif, especially if these ridges are indeed "rider blocks" on a larger and probably older detachment system.

4.4. Evolution of the Eastern Flank and Hydrothermal Activity

Some dating of hydrothermal precipitates has been carried out (Lalou et al., 1993, 1995, 1998), providing a frame for the development and evolution of the hydrothermal mounds. However, the observations during the M127 cruise showed that the TAG hydrothermal field comprises additional hydrothermal mounds and that distinct morphological differences related to the evolution of the various parts of the vent field also occur.

The oldest structural unit found in the high-resolution bathymetric data is the uplifted sedimented hummocky terrain in the south-east corner of the working area, at a water depth of 2,800 m (Figure 8). This volcanic terrain was formed 300 to 400 ka (based on the half-spreading rate of 13 mm/yr, McGregor et al., 1977) at the valley floor in a similar setting to the current extensional zone, as indicated by the similar fault pattern. With the initiation of the major bounding fault, during a pronounced tectonic phase, this terrain was

uplifted by more than 800 m into the upper section of the eastern flank. During this exhumation, the upper faulted terrain was created in the north by continuous normal and transfer faulting. This episode could also be related to the initiation of the detachment fault and the onset of the exhumation of the corrugated surface by the rotation of a normal fault due to localized stress. A following magmatic phase created the Mir block, the smooth northern block, and likely parts of the chaotic zone. These blocks were subsequently uplifted along normal faults and, in the case of the smooth northern block, likely dragged onto the detachment surface. During the uplift, these blocks were also highly tectonized and partially covered by mass-wasting products.

The general structural pattern and the distance to the spreading axis imply that the tectonized areas and the unfissured sections of the hanging wall were largely formed during the same magmatic episode. Even though the ponded flow is not affected by the different fault populations and therefore appears to be young, visual observations (Murton et al., 2018) showed a sediment cover of at least 10–15 cm on top of the lake, which is similar to the sediment depth observed in gravity core samples taken west of the active mound (Petersen & Shipboard Scientific Party, 2016). Hence, there seems to be no major age progression in the volcanic terrain with distance to the spreading axis in this small area. The magmatic phase that formed the main part of the hydrothermal field was succeeded by a phase of ridge-parallel extensional faulting in the eastern part of the valley floor. Unequal movement between the exhumation of the northern detachment, the Mir block, and the valley floor is accommodated in the chaotic zone, resulting in its rough appearance.

The most recent magmatic phase led to the formation of the neovolcanic ridges in the center of the axial valley observed in the ship-based data sets (Figure 3). Magmatic activity at the neovolcanic ridges southwest of the hydrothermal field may be related to the propagation of dikes, which intruded along predefined weak zones into the southern area of the hydrothermal field. These dikes may be associated with the small percentage of observed extrusive fissures (Bohnenstiehl & Kleinrock, 2000). Phases of extensional faulting alternated with axis oblique faulting and fracturing, possibly due to shifts in the dominant stress regime. A recent episode of tectonic extension may have led to the rejuvenation of major axis parallel extensional faults east of the active mound (Figure 4).

Manganese-oxyhydroxides are the oldest hydrothermal material from the entire TAG hydrothermal field (about 140 ka) and were recovered from the periphery of the Mir Mound. Hence, hydrothermal activity likely started in the east of the valley floor when the Mir Zone was in a distance to the spreading axis similar to the position of the active TAG mound today. The Mir Zone shows signs of oblique and axis perpendicular faulting, but it seems that the block largely stayed intact after the uplift in the lower valley wall and escaped the deviating tectonic stresses.

In contrast, the highly dissected and sedimented nature of Southern Mound, Double Mound and Rona Mound indicates that these mounds have formed between the uplift of the eastern blocks and the strong spreading-parallel extensional faulting. Shinkai and the smaller New Mounds seem to be spared from this extensional faulting even though they are located only 500 m to the west of the highly faulted mounds. Shinkai and the New Mounds were therefore likely formed after the extensional period that dissected the other mounds in the east. This is in agreement with the unsedimented nature of these mounds that also infers a younger age of the mounds in the west. Unfortunately, there is no published age data for Shinkai or the New Mounds. However, if Shinkai formed during the same time as Southern and Double Mound we would expect a different shape and that the smaller New Mounds would also show some evidence of faulting. Therefore, Shinkai and the two New Mounds might be younger than 40 ka, the youngest age of sulfides reported from the faulted eastern mounds (Double Mound; Lalou et al., 1995). The formation of the steep sulfide mounds in the west might rather correlate with some of the later stages of activity reported for the active TAG mound (excluding the most recent activity pulse that started ~80 years ago). Also, Mount de Reliques and mound #24 seem to be unfaulted and appear to be younger than the adjacent Double Mound. Therefore, they might indicate later stages of hydrothermal activity even in the chaotic zone. However, it should be kept in mind that sampling and age dating was scarce and might not be representative for the highly faulted Double and Southern mounds.

Visual observations from the lower terrace of the active TAG mound (Rona et al., 1986) indicate that venting is often linked to fractures rather than discrete discharge. This and recent fractures in the sedimented areas

just east of the mound suggest recent tectonic activity (Kleinrock & Humphris, 1996a). However, Kong et al. (1992) detected no earthquakes in the immediate vicinity of the active hydrothermal mound or beneath the actively developing faults to the east. The nearest recorded events were reported more than 2 km away and at depths exceeding 4.5 km below seafloor. Earthquakes detected by Pontbriand and Sohn (2014) close to the active mound are very small and are likely related to the precipitation of anhydrite within the mound and not associated with tectonic activity.

4.5. Tonnage Considerations

We infer a total sulfide tonnage of about 29 Mt (including 6.7 Mt in the stockwork zones) to be present in the active, weakly active, and inactive sulfide mounds of the TAG vent field (Table 2). This estimate is based on the volume calculations derived from the AUV-based high-resolution topography and assuming a density of 3.5 t/m^3. We can test our estimate by comparing it with published tonnage information obtained by drilling of the TAG active mound in 1994. Hannington et al. (1998) reported that 2.7 million tons of sulfide are present in the mound itself with an additional 1.2 million tons contained in the stockwork zone. Their calculations were based on an average density of 3.8 t/m^3 determined by Ludwig et al. (1998) on the drill core samples. Our calculation for the TAG active mound indicates a tonnage of 2.3 million tons above the reference surface. This is only slightly lower than the estimate of Hannington et al. (1998) and mainly a result of a slightly lower mound volume (647,000 m^3 versus ~700,000 m^3) and the lower density used in our calculations (3.5 t/m^3). We, therefore, assume our tonnage estimate for the entire hydrothermal field (29 Mt) to be a reasonable estimate. Overall, these 29 Mt are a significant portion of the roughly 600 million tons of sulfide assumed to be present within the neovolcanic zone of the global mid-ocean ridges (Hannington et al., 2010, 2011). Therefore, the TAG segment hosts a significant proportion (~5%) of the global estimate for the neovolcanic zones, which is substantially larger than most SMS deposits known to date (Hannington et al., 2010). It should also be noted that the presence of additional unknown hydrothermal mounds within the TAG hydrothermal field is likely, as some potential targets could not be investigated further due to time constraints. Their presence would increase the total accumulation of sulfide material even more. It is still unknown whether this elevated tonnage is a unique attribute of the TAG hydrothermal field, due to its tectonically complex regional and local geological setting, or if it is instead related to a lack of detailed investigations in other hydrothermal systems thereby underestimating their tonnages.

Studies from the Central Indian Ridge, also report significant sulfide occurrences from short, tectonically complex ridge segments (e.g., Kairei and Edmond vent fields, Okino et al., 2015; Van Dover et al., 2001), indicating that the tectonic history of a ridge segment plays an important role in the accumulation of sulfides. Furthermore, the estimated 600 Mt global tonnage is a representation of mainly active sites in the neovolcanic zones (~1,000 sites) and does not reflect the potential of SMS occurrences on the entire seafloor (Hannington et al., 2010, 2011). Studies from other hydrothermal fields in the Atlantic, Indian Ocean, and the Pacific have shown that with an increasing number of high-resolution surveys in the vicinity of known deposits, more inactive deposits are being discovered (Jamieson et al., 2014; Paduan et al., 2018).

The tonnage reported here for the TAG hydrothermal field is comparable to values reported for ophiolite-hosted mining districts on Cyprus, where single deposits have tonnages of 0.05 to 16 Mt (Hannington et al., 1998). However, the tonnages are substantially lower than values reported from other large mining districts on land (e.g., Abitibi Greenstone Belt, Canada). The amount of sulfide-dominated hydrothermal material within the TAG hydrothermal field amounts to an average of 630 kt/km^2, based on an area of 47 km^2. However, this value is calculated based on the entire area mapped by the AUV, which does not necessarily represent the extent of the hydrothermal field. Calculating the tonnage in relation to the smallest rectangular dimensions possible for the vent field that includes all known mounds (~14 km^2), would increase the potential ore volume to about 2.1 Mt/km^2. These values are higher than the values reported from the Endeavor Segment of 0.02 Mt/km^2 (Jamieson et al., 2014).

Assuming an average metal content in the inactive mounds similar to that drilled at the active TAG mound (Cu 2.8%, Zn 0.4%, Ag 14 ppm, Au 0.53 ppm; $N = 45$; Hannington et al., 1998) the field would comprise 804 kt Cu, 110 kt Zn, 402 t Ag, and 15.2 t Au. We use here the weighted average metal content of Hannington et al. (1998) for the interior of the TAG active mound due to a lack in sampling from the interior of the weakly active and inactive mounds. Only a few sulfide samples have been drilled from the upper parts of Southern

Mound, Rona Mound, and the Mir Mound in 2016 (Lehrmann et al., 2018; Murton et al., 2019) and their geochemical composition is likely, not representative for the entire mounds. Murton et al. (2019) report copper concentrations averaging 3.1 wt.% Cu ($N = 19$); however, they show clear variations between the mounds. A single sample from Southern Mound has 1.0 wt.% Cu, while average concentrations of 1.5 wt.% Cu at Rona Mound ($N = 14$) and 9.5 wt.% at Mir Mound ($N = 4$) are reported. With the exception of a single sample from Rona Mound (8.4 wt.% Zn) the drill core sample suite is characterized by low Zn concentrations and averages 0.6 wt.% Zn ($N = 19$). These values are slightly higher than the average value for the interior of the TAG mound, mostly because of a few high-grade samples from the Mir and Rona mounds. Due to the low sample number and the limited penetration into the mounds we consider the average grade from the TAG active mound published by Hannington et al. (1998) to be a more reasonable estimate for the bulk composition of the inactive and weakly active mounds. Using these metal grades, the surface metal density for the TAG area would be just over 20.000 t Cu + Zn/km^2. These values for the TAG field, however, only include the identified hydrothermal mounds and do not account for any potential accumulation of sulfides in the metalliferous sediments surrounding the mounds or the thick (2–3 m) Cu-rich sediments in the channel-like depression in the deepest parts of the trough south of Rona Mound (Figures 8 and 10a). The latter was observed in gravity core samples retrieved during cruises M127 and JC138 (Murton et al., 2019; Petersen & Shipboard Scientific Party, 2016). The lateral extent of these metalliferous sediments is not known. However, based on the topography, the retrieved sediment cores, and observations made during M127 and JC138 we inferred that thick hydrothermal sediments occur in the surroundings of all larger mounds (Figure 10), commonly below a layer of pelagic sediment. The channel-like depression likely received input through mass transport of sulfides and other hydrothermal components from the erosion of the adjacent Southern, Rona, and Abyss mounds, but probably even from the distal Mir Zone (indicated by the white arrows in Figure 10).

4.6. Sulfide Accumulation Rates

Assuming a constant spreading rate (12–13 mm/yr) over the last 500,000 years, the crust hosting the oldest known sulfides in the TAG vent field around the Mir Zone (4 km distance to the spreading center), may not be older than 300,000 years. Our results indicate that sulfide formation is related to large scale faulting following this volcanic phase. The oldest record of hydrothermal activity in the area, determined from hydrothermal manganese crusts collected at the Mir Mound and from the low-temperature zone in the east, indicates a minimum age of hydrothermal activity of 125,000 to 140,000 years (Lalou et al., 1986, 1993). Dating of hydrothermal precipitates indicates that high-temperature sulfide formation at the Mir Mound started around 100,000 years ago (Lalou et al., 1993). The formation of 29 Mt of sulfides in a 100,000-year period would result in an accumulation rate of ~300 t/yr. However, episodic hydrothermal venting has been proposed by age gaps identified from dating of the hydrothermal deposits in the area. Lalou et al. (1995) suggest that, over a ~50,000-year history, hydrothermal activity at the active TAG mound has been confined to only 20% of this time. If we assume a similar episodic activity for the other inactive sulfide mounds, sulfide accumulation rates for the entire field over the last 100,000 years could amount to ~1,500 t/yr during ~20,000 years of hydrothermal activity. This rate lies above the published range of estimated accumulation rates that vary from 1 to 800 t/yr (compiled in Jamieson et al., 2014) that include everything from individual black smokers to entire vent fields. Hannington et al. (1998) calculated a value of between 500 and 1,000 t/yr for periods of hydrothermal activity at the active TAG mound, while the accumulation rate for all active and inactive sulfides along the entire Endeavor Segment was estimated to be about 400 t/yr (Jamieson et al., 2014). The sulfide accumulation rate within the entire TAG hydrothermal field is likely not significantly higher than that of other hydrothermal systems. However, it is the duration of hydrothermal activity in a confined area that raises the sulfide tonnage at the TAG hydrothermal field above average when compared to other vent fields.

5. Conclusions

By combining multiresolution bathymetric data sets, we were able to significantly advance our understanding of the relationships between the volcanic, tectonic, and hydrothermal features and processes associated with the TAG hydrothermal field. Our conclusions can be summarized as follows.

1. The active TAG mound and the sulfide mounds in the Three Mound area are located at the intersection of different fault and fissure populations that mark distinct tectonic zones that relate to temporal changes in the prevailant stress regime.
2. The presence of a corrugated surface in the north of the field adds complexity to the structural control on hydrothermal venting and contributes to its longevity.
3. The Mir Mound, Southern Mound, and Shimmering Mound are located close to major faults that might intersect the detachment faults at depth, enabling the low-temperature hydrothermal activity.
4. The inactive to weakly active sulfide mounds are of different age indicating temporal and regional variability in the location of upflow zones from an undefined heat source at depth.
5. The estimated sulfide tonnage for the TAG vent field is ~29 Mt, including an estimated 30% of subsurface stockwork mineralization. Most (~90%) of the hydrothermal material lies in inactive and weakly active sulfide mounds, highlighting the importance of developing new exploration methods that do not rely on water column anomalies caused by a buoyant plume.
6. The location of the inactive and weakly active mounds along the margin of a larger detachment system and the discovery of new mounds during cruise M127 indicates that there is still potential for further discoveries within the area and possibly even further off-axis between the large ridges further to the east.
7. The calculated sulfide accumulation rate is ~1.500 t/yr, assuming that hydrothermal activity occurred only during 20% of the estimated 100,000-year history of venting at this site, and is higher than that reported from other modern seafloor vent fields. However, the TAG vent field is not characterized by a different and more powerful type of hydrothermal activity. It is the tectonic control and longevity of the system that confines sulfide formation into a small area.

There is a need to extend the survey area to the north and east away from the axis in order to fully quantify the extent of hydrothermal deposition. This would also provide additional information about the evolution of the eastern flank and the geographic extent of the hydrothermal convection cell. Petrological sampling along the eastern wall is lacking and would help in reconstructing the tectonic evolution of the TAG segment. Further investigations in the sedimented areas between the large, linear ridges to the east may also provide information about the sequence of hydrothermal activity and shed light on possible hydrothermal activity east of the known TAG vent field.

Data Availability Statement

The ship-based and the AUV bathymetric data are publicly available on the PANGAEA data repository (doi.org/10.1594/PANGAEA.899408 and doi.org/10.1594/PANGAEA.899415). GMRT bathymetric data were downloaded from this site (https://www.gmrt.org/GMRTMapTool/).

Acknowledgments

This study is based on data collected during research cruise M127, which was part of the EU-funded project "Blue mining: Breakthrough Solutions for the Sustainable Deep Sea Mining Value Chain" (Grant 604500). We would like to thank the crew of the RV Meteor and the GEOMAR AUV team for their hard work and professionalism, which enabled us to collect all data necessary for this study. We also thank all members of the scientific team who participated in the collection and processing of the data. Further, we would also like to thank the reviewer William Chadwick and an additional anonymous reviewer for their valuable and thoughtful comments, which helped to improve the manuscript. J. W. J. acknowledges funding from the Canada Research Chair Program.

References

Beaulieu, S. E., Baker, E. T., & German, C. R. (2015). Where are the undiscovered hydrothermal vents on oceanic spreading ridges? *Deep Sea Research Part II: Topical Studies in Oceanography*, *121*, 202–212. https://doi.org/10.1016/j.dsr2.2015.05.001

Beaulieu, S. E., Baker, E. T., German, C. R., & Maffei, A. (2013). An authoritative global database for active submarine hydrothermal vent fields. *Geochemistry, Geophysics, Geosystems*, *14*, 4892–4905. https://doi.org/10.1002/2013GC004998

Blackman, D. K., Cann, J. R., Janssen, B., & Smith, D. K. (1998). Origin of extensional core complexes: Evidence from the Mid-Atlantic Ridge at Atlantis fracture zone. *Journal of Geophysical Research*, *103*(B9), 21,315–21,333. https://doi.org/10.1029/98JB01756

Bohnenstiehl, D. R., & Kleinrock, M. C. (1999). Faulting and fault scaling on the median valley floor of the trans-Atlantic geotraverse (TAG) segment, ~26°N on the Mid-Atlantic Ridge. *Journal of Geophysical Research*, *104*, 29,351–29,364. https://doi.org/10.1029/1999JB900256

Bohnenstiehl, D. R., & Kleinrock, M. C. (2000). Fissuring near the TAG active hydrothermal mound, 26°N on the Mid-Atlantic Ridge. *Journal of Volcanology and Geothermal Research*, *98*, 33–48. https://doi.org/10.1016/S0377-0273(99)00192-4

Canales, J. P., Sohn, R. A., & DeMartin, B. J. (2007). Crustal structure of the Trans-Atlantic Geotraverse (TAG) segment (Mid-Atlantic Ridge, 26°10′N): Implications for the nature of hydrothermal circulation and detachment faulting at slow spreading ridges. *Geochemistry, Geophysics, Geosystems*, *8*, Q08004. https://doi.org/10.1029/2007GC001629

Cann, J. R., Smith, D. K., Escartín, J., & Schouten, H. (2015). Tectonic evolution of 200 km of Mid-Atlantic Ridge over 10 million years: Interplay of volcanism and faulting. *Geochemistry, Geophysics, Geosystems*, *16*, 2303–2321. https://doi.org/10.1002/2015GC005797

Cannat, M., Mangeney, A., Ondréas, H., Fouquet, Y., & Normand, A. (2013). High-resolution bathymetry reveals contrasting landslide activity shaping the walls of the Mid-Atlantic Ridge axial valley. *Geochemistry, Geophysics, Geosystems*, *14*, 996–1011. https://doi.org/10.1002/ggge.20056

Caress, D. W. (1999). *MB-System—Public domain software for processing swath mapping sonar data: Undersea explorations*.

Cathles, L. M. (2011). What processes at mid-ocean ridges tell us about volcanogenic massive sulfide deposits. *Mineralium Deposita*, *46*, 639–657. https://doi.org/10.1007/s00126-010-0292-9

Cherkashev, G. A., Ivanov, V. N., Bel'tenev, V. I., Lazareva, L. I., Rozhdestvenskaya, I. I., Samovarov, M. L., et al. (2013). Massive sulfide ores of the northern equatorial Mid-Atlantic Ridge. *Oceanology*, *53*(5), 607–619. https://doi.org/10.1134/S0001437013050032

Clague, D. A., Caress, D. W., Dreyer, B. M., Lundsten, L., Paduan, J. B., Portner, R. A., et al. (2018). Geology of the Alarcon Rise, southern Gulf of California. *Geochemistry, Geophysics, Geosystems*, *19*, 807–837. https://doi.org/10.1002/2017GC007348

DeMartin, B. J., Sohn, R. A., Canales, J. P., & Humphris, S. E. (2007). Kinematics and geometry of active detachment faulting beneath the TAG hydrothermal field on the Mid-Atlantic Ridge. *Geology*, *35*, 711–741. https://doi.org/10.1130/G23718A.1

Escartín, J., Mével, C., MacLeod, C. J., & McCaig, A. M. (2003). Constraints on deformation conditions and the origin of oceanic detachments: The Mid-Atlantic Ridge core complex at 15°45′N. *Geochemistry, Geophysics, Geosystems*, *4*(8), 1067. https://doi.org/10.1029/2002GC000472

Escartín, J., Mével, C., Petersen, S., Bonnemains, D., Cannat, M., Andreani, M., et al. (2017). Tectonic structure, evolution, and the nature of oceanic core complexes and their detachment fault zones (13°20′N and 13°30′N, mid Atlantic ridge). *Geochemistry, Geophysics, Geosystems*, *18*, 1451–1482. https://doi.org/10.1002/2016GC006775

Francheteau, J., Needham, H. D., Choukroune, P., Juteau, T., Seguret, M., Ballard, R. D., et al. (1979). Massive deep-sea sulphide ore deposits discovered on the East Pacific rise. *Nature*, *277*(5697), 523–528. https://doi.org/10.1038/277523a0

German, C. R., Casciotti, K. A., Dutay, J.-C., Heimbürger, L. E., Jenkins, W. J., Measures, C. I., et al. (2016). Hydrothermal impacts on trace element and isotope ocean biogeochemistry. *Philosophical Transactions of the Royal Society A - Mathematical Physical and Engineering Sciences*, *374*(2081), 20160035. https://doi.org/10.1098/rsta.2016.0035

Golder Associates Pty. Ltd (2012). *Mineral resource estimate, Solwara project, Bismarck Sea, PNG: Technical report compiled under NI43–101, submitted to Nautilus Minerals Nuigini Limited as SL01-NSG-RPT-7020-001 Rev 1, Golder Resource Report*. Retrieved from https://sec.report/otc/financial-report/78790

Gudmundsson, A. (1990). Emplacement of dikes, sills and crustal magma chambers at divergent plate boundaries. *Tectonophysics*, *176*, 257–275. https://doi.org/10.1016/0040-1951(90)90073-H

Gudmundsson, A. (1998). Magma chamber modeled as cavities explain the formation of rift zone central volcanoes and their eruption and intrusion statistics. *Journal of Geophysical Research*, *103*(B4), 7401–7412. https://doi.org/10.1029/97JB03747

Hannington, M. D., Galley, A. G., Herzig, P. M., & Petersen, S. (1998). Comparison of the TAG mound and stockwork complex with Cyprus-type massive sulfide deposits. In P. M. Herzig, S. E. Humphris, D. J. Miller, & R. A. Zierenberg (Eds.), *Proceedings of the ocean drilling program, scientific results* (Vol. 158, pp. 389–415). College Station, TX: Ocean Drilling Program.

Hannington, M. D., Jamieson, J., Monecke, T., & Petersen, S. (2010). Modern sea-floor massive sulfides and base metal resources: Toward an estimate of global sea-floor massive sulfide potential. In R. J. Goldfarb, E. E. Marsh, & T. Monecke (Eds.), *The challenge of finding new mineral resources: Global metallogeny, innovative exploration, and new discoveries*, *Vol. 2: Zinc-Lead, Nickel-Copper-PGE, and Uranium* (pp. 317–338). Littleton, Colorado: Special publications of the Society of Economic Geologists (15). Society of Economic Geologists.

Hannington, M. D., Jamieson, J., Monecke, T., Petersen, S., & Beaulieu, S. (2011). The abundance of seafloor massive sulfide deposits. *Geology*, *39*, 1155–1158. https://doi.org/10.1130/G32468.1

Hekinian, R., Fevrier, M., Bischoff, J. L., Picot, P., & Shanks, W. C. (1980). Sulfide deposits from the East Pacific rise near 21°N. *Science*, *207*(4438), 1433–1444. https://doi.org/10.1126/science.207.4438.1433

Humphris, S. E., Herzig, P. M., Miller, D. J., & Shipboard Scientific Party (1996). Proceedings of the ODP, Initial Reports (p. 158), Ocean Drilling Program, College Station, TX.

Humphris, S. E., Tivey, M. K., & Tivey, M. A. (2015). The trans-Atlantic Geotraverse hydrothermal field: A hydrothermal system on an active detachment fault. *Deep Sea Research Part II: Topical Studies in Oceanography*, *121*, 8–16. https://doi.org/10.1016/j.dsr2.2015.02.015

Jamieson, J. W., Clague, D. A., & Hannington, M. D. (2014). Hydrothermal sulfide accumulation along the Endeavour segment, Juan de Fuca Ridge. *Earth and Planetary Science Letters*, *395*, 136–148. https://doi.org/10.1016/j.epsl.2014.03.035

Karson, J. A., & Rona, P. A. (1990). Block-tilting, transfer faults, and structural control of magmatic and hydrothermal processes in the TAG area, Mid-Atlantic Ridge 26°N. *Geological Society of America Bulletin*, *102*, 1635–1645. https://doi.org/10.1130/0016-7606(1990)102<1635:BTTFAS>2.3.CO;2

Kleinrock, M. C., & Humphris, S. E. (1996a). Structural asymmetry of the TAG Rift Valley: Evidence from a near-bottom survey for episodic spreading. *Geophysical Research Letters*, *23*(23), 3439–3442. https://doi.org/10.1029/96GL03073

Kleinrock, M. C., & Humphris, S. E. (1996b). Structural control on sea-floor hydrothermal activity at the TAG active mound. *Nature*, *382*(6587), 149–153. https://doi.org/10.1038/382149a0

Kleinrock, M. C., Humphris, S. E., Shaw, P., Bowen, A., Crook, T., Davis, C., et al. (1996). Detailed structure and morphology of the tag active hydrothermal mound and its geotectonic environment. In *Proceedings from the Ocean Drilling Program, Initial Reports* (Vol. 158, pp. 15–21). College Station, TX: Ocean Drilling Program.

Kong, L. S. L., Solomon, S. C., & Purdy, G. M. (1992). Microearthquake characteristics of a mid-ocean ridge along-axis high. *Journal of Geophysical Research*, *97*, 1659–1685. https://doi.org/10.1029/91JB02566

Lalou, C., Reyss, J. L., & Brichet, E. (1998). Age of sub-bottom sulfide samples at the TAG active mound. In P. M. Herzig, S. E. Humphris, D. J. Miller, & R. A. Zierenberg (Eds.), *Proceedings of the Ocean Drilling Program, Scientific Results* (Vol. 158, pp. 111–117). College Station, TX: Ocean Drilling Program.

Lalou, C., Reyss, J.-L., Brichet, E., Arnold, M., Thompson, G., Fouquet, Y., & Rona, P. A. (1993). New age data for Mid-Atlantic Ridge hydrothermal sites: TAG and Snakepit chronology revisited. *Journal of Geophysical Research*, *98*, 9705–9713. https://doi.org/10.1029/92JB01898

Lalou, C., Reyss, J.-L., Brichet, E., Rona, P. A., & Thompson, G. (1995). Hydrothermal activity on a 10^5-year scale at a slow-spreading ridge, TAG hydrothermal field, Mid-Atlantic Ridge 26°N. *Journal of Geophysical Research*, *100*(B9), 17,855–17,862. https://doi.org/10.1029/95JB01858

Lalou, C., Thompson, G., Rona, P. A., Brichet, E., & Jehanno, C. (1986). Chronology of selected hydrothermal Mn oxide deposits from the transatlantic geotraverse "TAG" area, Mid-Atlantic ridge 26°N. *Geochimica et Cosmochimica Acta*, *50*, 1737–1743. https://doi.org/10.1016/0016-7037(86)90135-3

Lehrmann, B., Stobbs, J. I., Lusty, A. P., & Murton, J. B. (2018). Insights into extinct seafloor massive sulfide mounds at the TAG, Mid-Atlantic ridge. *Minerals*, *8*, 302. https://doi.org/10.3390/min8070302

Lisitsyn, A. P., Bogdanov, Y. A., Zonenshayn, L. P., Kuz'min, M. I., & Sagalevich, A. M. (1989). Hydrothermal phenomena in the Mid-Atlantic ridge at lat. 26°N (TAG hydrothermal field). *International Geology Review*, *31*(12), 1183–1198. https://doi.org/10.1080/00206818909465971

Ludwig, R. J., Iturrino, G. J., & Rona, P. A. (1998). Seismic velocity-porosity relationship of sulfide, sulfate and basalt samples from the TAG hydrothermal mound. In P. M. Herzig, S. E. Humphris, D. J. Miller, & R. A. Zierenberg (Eds.), *Proceedings of the Ocean Drilling Program, Scientific Results* (Vol. 158, pp. 313–327). College Station, TX: Ocean Drilling Program.

MacLeod, C. J., Searle, R. C., Murton, B. J., Casey, J. F., Mallows, C., Unsworth, S. C., et al. (2009). Life cycle of oceanic core complexes. *Earth and Planetary Science Letters*, *287*(3–4), 333–344. https://doi.org/10.1016/j.epsl.2009.08.016

McCaig, A. M., Cliff, R. A., Escartín, J., Fallick, A. E., & MacLeod, C. J. (2007). Oceanic detachment faults focus very large volumes of black smoker fluids. *Geology*, *35*, 935–938. https://doi.org/10.1130/G23657A.1

McCaig, A. M., Delacour, A., Fallick, A. E., Castelain, T., & Früh-Green, G. L. (2013). Detachment fault control on hydrothermal circulation systems: Interpreting the subsurface beneath the TAG hydrothermal field using the isotopic and geological evolution of oceanic core complexes in the Atlantic. *Geophysical Monograph Series*, *188*, 207–239. https://doi.org/10.1029/2008GM000729

McGregor, B., Harrison, C., William Lavelle, J. A., & Rona, P. (1977). Magnetic anomaly patterns on Mid-Atlantic ridge crest at 26°N. *Journal of Geophysical Research*, *82*, 231–238. https://doi.org/10.1029/JB082i002p00231

Müller, H., Schwalenberg, K., Reeck, K., Barckhausen, U., Schwarz-Schampera, U., Hilgenfeldt, C., & von Dobeneck, T. (2018). Mapping seafloor massive sulfides with the Golden Eye frequency-domain EM profiler. *First Break*, *36*, 61–67.

Murton, B. J., Lehrmann, B., Dutrieux, A. M., Martins, S., de la Iglesia, A. G., Stobbs, I. J., et al. (2019). Geological fate of seafloor massive sulphides at the TAG hydrothermal field (Mid-Atlantic ridge). *Ore Geology Reviews*, *107*, 903–925. https://doi.org/10.1016/j.oregeorev.2019.03.005

Murton, J. B., & Lusty, P. (2018). *Cruise report RRS James Cook JC138, Blue Mining Project*. National Oceanography Centre.

Okino, K., Nakamura, K., & Sato, H. (2015). Tectonic background of four hydrothermal fields along the Central Indian ridge. In J. Ishibashi, K. Okino, & M. Sunamura (Eds.), *Subseafloor biosphere linked to hydrothermal systems: TAIGA concept* (pp. 133–146). Tokyo: Springer Japan.

Olive, J.-A., Parnell-Turner, R., Escartín, J., Smith, D. K., & Petersen, S. (2019). Controls on the seafloor exposure of detachment fault surfaces. *Earth and Planetary Science Letters*, *506*, 381–387. https://doi.org/10.1016/j.epsl.2018.11.001

Paduan, J. B., Zierenberg, R. A., Clague, D. A., Spelz, R. M., Caress, D. W., Troni, G., et al. (2018). Discovery of hydrothermal vent fields on Alarcón rise and in southern Pescadero Basin, Gulf of California. *Geochemistry, Geophysics, Geosystems*, *19*, 4788–4819. https://doi.org/10.1029/2018GC007771

Petersen, S., Herzig, P. M., & Hannington, M. D. (2000). Third dimension of a presently forming VMS deposit: TAG hydrothermal mound, Mid-Atlantic ridge, 26°N. *Mineralium Deposita*, *35*, 233–259. https://doi.org/10.1007/s001260050018

Petersen, S., Krätschell, A., Augustin, N., Jamieson, J., Hein, J. R., & Hannington, M. D. (2016). News from the seabed—Geological characteristics and resource potential of deep-sea mineral resources. *Marine Policy*, *70*, 175–187. https://doi.org/10.1016/j.marpol.2016.03.012

Petersen, S., & Shipboard Scientific Party (2016). *Metal fluxes and resource potential at the slow-spreading TAG midocean ridge segment (26°N, MAR), Cruisereport M127*.

Pontbriand, C. W., & Sohn, R. A. (2014). Microearthquake evidence for reaction-driven cracking within the trans-Atlantic Geotraverse active hydrothermal deposit. *Journal of Geophysical Research: Solid Earth*, *119*, 822–839. https://doi.org/10.1002/2013JB010110

Purdy, G. M., Sempéré, J.-C., Schouten, H., Dubois, D. L., & Goldsmith, R. (1990). Bathymetry of the Mid-Atlantic Ridge, 24°–31°N: A map series. *Marine Geophysical Researches*, *12*, 247–252. https://doi.org/10.1007/BF02428196

QGIS Development Team (2019). QGIS geographic information system, open source Geospatial Foundation project, version 3.8.0, Zanzibar. Retrieved from https://qgis.org

Ranero, C. R., & Reston, T. J. (1999). Detachment faulting at ocean core complexes. *Geology*, *27*, 983–986. https://doi.org/10.1130/0091-7613(1999)027<0983:DFAOCC>2.3.CO;2

Reston, T. J., & Ranero, C. R. (2011). The 3-D geometry of detachment faulting at mid-ocean ridges. *Geochemistry, Geophysics, Geosystems*, *12*, Q0AG05. https://doi.org/10.1029/2011GC003666

Rona, P. A. (1976). Pattern of hydrothermal mineral deposition: Mid-Atlantic ridge crest at latitude 26°N. *Marine Geology*, *21*, M59–M66. https://doi.org/10.1016/0025-3227(76)90009-8

Rona, P. A. (2003). Resources of the sea floor. *Science*, *299*, 673–674. https://doi.org/10.1126/science.1080679

Rona, P. A., Bogdanov, Y., Gurvich, E. G., Rimski-Korsakov, N., Sagalevitch, A. M., Hannington, M. D., & Thompson, G. (1993). Relict hydrothermal zones in the TAG hydrothermal field, Mid-Atlantic ridge 26°N, 45°W. *Journal of Geophysical Research*, *98*(B6), 9715–9730. https://doi.org/10.1029/93JB00552

Rona, P. A., Hannington, M. D., Raman, C. V., Thompson, G., Tivey, M. K., Humphris, S. E., et al. (1993). Active and relict sea-floor hydrothermal mineralization at the TAG hydrothermal field, Mid-Atlantic Ridge. *Economic Geology*, *88*(8), 1989–2017. https://doi.org/10.2113/gsecongeo.88.8.1989

Rona, P. A., Klinkhammer, G., Nelsen, T. A., Trefry, J. H., & Elderfield, H. (1986). Black smokers, massive sulphides and vent biota at the Mid-Atlantic ridge. *Nature*, *321*, 33–37. https://doi.org/10.1038/321033a0

Rona, P. A., Thompson, G., Mottl, M. J., Karson, J. A., Jenkins, W. J., Graham, D., et al. (1984). Hydrothermal activity at the trans-Atlantic Geotraverse hydrothermal field, Mid-Atlantic Ridge crest at 26°N. *Journal of Geophysical Research*, *89*(B13), 11,365–11,377. https://doi.org/10.1029/JB089iB13p11365

Ryan, W. B. F., Carbotte, S. M., Coplan, J. O., O'Hara, S., Melkonian, A., Arko, R., et al. (2009). Global multi-resolution topography synthesis. *Geochemistry, Geophysics, Geosystems*, *10*, Q03014. https://doi.org/10.1029/2008GC002332

Sangster, D. F. (1980). Quantitative characteristics of volcanogenic massive sulfide deposits I. Metal content and size distribution of massive sulphide deposits in volcanic centers. *CIM Bulletin*, *73*, 74–81.

Schouten, H., Smith, D. K., Cann, J. R., & Escartín, J. (2010). Tectonic versus magmatic extension in the presence of core complexes at slow-spreading ridges from a visualization of faulted seafloor topography. *Geology*, *38*, 615–618. https://doi.org/10.1130/G30803.1

Scott, M. R., Scott, R. B., Morse, J. W., Betzer, P. R., Butler, L. W., & Rona, P. A. (1978). Metal-enriched sediments from the TAG hydrothermal field. *Nature*, *276*, 811–813. https://doi.org/10.1038/276811a0

Sempéré, J.-C., Lin, J., Brown, H. S., Schouten, H., & Purdy, G. M. (1993). Segmentation and morphotectonic variations along a slow-spreading center: The Mid-Atlantic ridge (24°00′N–30°40′N). *Marine Geophysical Researches*, *15*, 153–200. https://doi.org/10.1007/BF01204232

Smith, D. K., Escartín, J., Schouten, H., & Cann, J. R. (2008). Fault rotation and core complex formation: Significant processes in seafloor formation at slow-spreading mid-ocean ridges (Mid-Atlantic Ridge, 13°–15°N). *Geochemistry, Geophysics, Geosystems*, *9*, Q03003. https://doi.org/10.1029/2007GC001699

Spagnoli, G., Hannington, M. D., Bairlein, K., Hördt, A., Jegen, M., Petersen, S., & Laurila, T. (2016). Electrical properties of seafloor massive sulfides. *Geo-Marine Letters*, *36*, 235–245. https://doi.org/10.1007/s00367-016-0439-5

Szitkar, F., Dyment, J., Petersen, S., Bialas, J., Klischies, M., Graber, S., et al. (2019). Detachment tectonics at Mid-Atlantic Ridge 26°N. *Scientific Reports*, *9*, 11830. https://doi.org/10.1038/s41598-019-47974-z

Tivey, M. A., Rona, P. A., & Schouten, H. (1993). Reduced crustal magnetization beneath the active mound, TAG hydrothermal field, Mid-Atlantic Ridge, at 26°N. *Earth and Planetary Science Letters*, *115*, 101–115. https://doi.org/10.1016/0012-821X(93)90216-V

Tivey, M. A., Schouten, H., & Kleinrock, M. C. (2003). A near-bottom magnetic survey of the Mid-Atlantic Ridge axis at 26°N: Implications for the tectonic evolution of the TAG segment. *Journal of Geophysical Research*, *108*(B5), 2277. https://doi.org/10.1029/2002JB001967

Tivey, M. K., Stakes, D. S., Cook, T. L., Hannington, M. D., & Petersen, S. (1999). A model for growth of steep-sided vent structures on the Endeavour segment of the Juan de Fuca ridge: Results of a petrologic and geochemical study. *Journal of Geophysical Research*, *104*(B10), 22,859–22,883. https://doi.org/10.1029/1999JB900107

Tucholke, B. E., & Lin, J. (1994). A geological model for the structure of ridge segments in slow spreading ocean crust. *Journal of Geophysical Research*, *99*(B6), 11,937–11,958. https://doi.org/10.1029/94JB00338

Van Dover, C. L., Arnaud-Haond, S., Gianni, M., Helmreich, S., Huber, J. A., Jaeckel, A. L., et al. (2018). Scientific rationale and international obligations for protection of active hydrothermal vent ecosystems from deep-sea mining. *Marine Policy*, *90*, 20–28. https://doi.org/10.1016/j.marpol.2018.01.020

Van Dover, C. L., Humphris, S. E., Fornari, D., Cavanaugh, C. M., Collier, R., Goffredi, S. K., et al. (2001). Biogeography and ecological setting of Indian Ocean hydrothermal vents. *Science*, *294*(5543), 818–823. https://doi.org/10.1126/science.1064574

White, S. N., Humphris, S. E., & Kleinrock, M. C. (1998). New observations on the distribution of past and present hydrothermal activity in the TAG area of the Mid-Atlantic Ridge (26°08′N). *Marine Geophysical Researches*, *20*, 41–56. https://doi.org/10.1023/A:1004376229719

Zhao, M., Canales, J. P., & Sohn, R. A. (2012). Three-dimensional seismic structure of a Mid-Atlantic Ridge segment characterized by active detachment faulting (Trans-Atlantic Geotraverse, 25°55′N-26°20′N). *Geochemistry, Geophysics, Geosystems*, *13*, Q0AG13. https://doi.org/10.1029/2012GC004454

Zonenshain, L. P., Kuzmin, M. I., Lisitsin, A. P., Bogdanov, Y. A., & Baranov, B. V. (1989). Tectonics of the Mid-Atlantic rift valley between the TAG and MARK areas (26–24°N): Evidence for vertical tectonism. *Tectonophysics*, *159*, 1–23. https://doi.org/10.1016/0040-1951(89)90167-4